AD-A061 309 NORTHROP RESEARCH AND TECHNOLOGY CENTER PALOS VERDES --ETC F/G 20/12
RADIATION EFFECTS ON CHARGE-COUPLED DEVICES AND OTHER MOS STRUC--ETC(U)
OCT 78 J R SROUR, S OTHMER, S C CHEN DAAG39-77-C-0134
UNCLASSIFIED NRTC-78-27R HDL-CR-78-134-1 NL

2 OF 2
AD
A061309

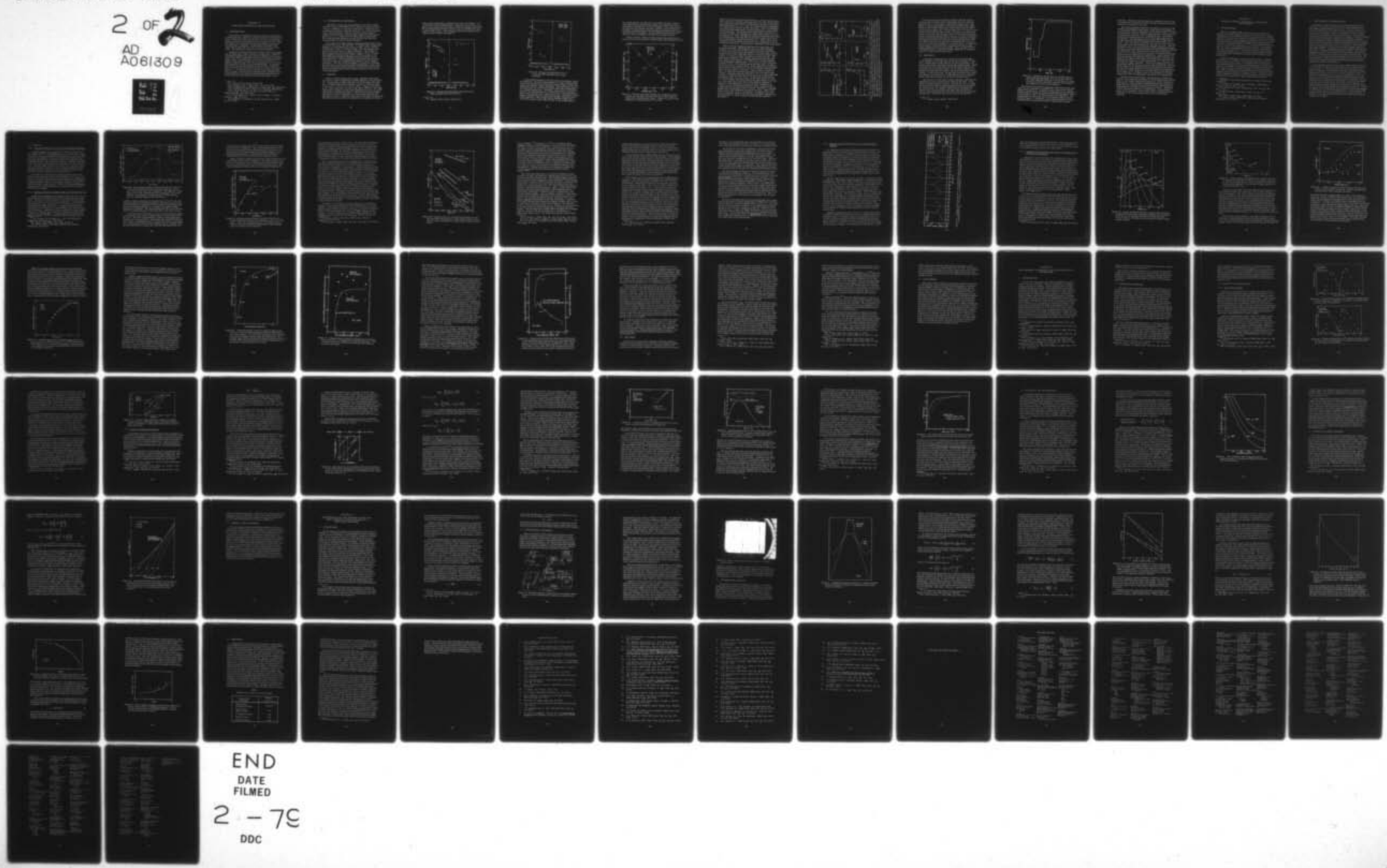

END
DATE
FILMED
2 - 79
DDC

SECTION 3.0

BIAS-STRESS EFFECTS IN MOS CAPACITORS

3.1 INTRODUCTION

In the course of studying the effects of neutron bombardment on MOS capacitors, which are reported in Section 2.0 of this document, certain bias-stress effects were observed. Specifically, biasing a device into strong inversion for a period of time caused the storage time, as determined from capacitance versus time measurements, to degrade. A subsequent accumulation bias caused the storage time to recover to near its pre-bias-stress value. This section describes our bias-stress findings.

Nakagiri[29] noted the production of interface states by application of a high field of either polarity to an SiO_2 film. Jeppson[30] investigated negative bias stress effects in MOS devices over the range 25 to 125°C at high fields and observed creation of interface states. Other related studies have also been performed.[31-34] Takino[10] reported on the effect of a bias stress on C-t curves for MOS capacitors on both n- and p-type substrates. The results presented herein are qualitatively similar to those of Takino in that an inversion bias is required to observe storage-time degradation; i.e., a negative bias is needed for n-type and a positive bias for p-type. Certain devices examined here exhibited orders-of-magnitude more of a bias-stress effect than that observed by Takino, whereas other devices yielded results similar to his.

---

[10] T. Takino, Ph.D. thesis, UCLA 1976.

[29] M. Nakagiri, Jap. J. Appl. Phys. 13, 1610 (1974).

[30] K.O. Jeppson and C.M.Svensson, J. Appl. Phys. 48, 2004 (1977).

[31] A. Goetzberger and H.E. Nigh, Proc. IEEE 54, 1454 (1966).

[32] B.E. Deal, M. Sklar, A.S. Grove, and E.H. Snow, J. Electrochem Soc. 114, 266 (1967).

[33] A. Goetzberger, A.D. Lopez, and R.J. Strain, J. Electrochem Soc. 120, 90 (1973).

[34] I. Kobayashi, M. Nakahara, and M. Atsumi, Proc. IEEE 61, 249 (1973).

3.2 EXPERIMENTAL PROCEDURE

Capacitance versus time measurements were made on MOS capacitors using a PAR Model 410 C-V System and were recorded on an x-y recorder or a storage oscilloscope. To measure C-t, a voltage step taking an n-type device from -5 to -10V was applied (+5 to +10V for p-type). Devices studied were fabricated by Hughes Aircraft and were from the same wafers described in Section 2.2.2.8, i.e., Wet N, Dry N, Wet P, Dry P, and KA-09. The metal electrode thickness was thin (650 Å) in the first four cases and thick (~1 μm) for the KA-09 wafer.

The values of DC bias applied to study degradation and recovery of storage time were ±10V and ±30V. To obtain a long storage time initially, an n-type device was biased at either +10V or +30V for several hours (-10V or -30V for p-type). The long-storage-time state is referred to here as "upper saturation." To achieve a short storage time in an n-type device, either -10V or -30V was then applied for several hours (+10V or +30V for p-type). The short-storage-time state eventually reached is termed "lower saturation" here. (This terminology is not strictly correct since an inversion bias was not applied long enough to reach complete saturation. The term "lower saturation" is used here to indicate that the rate of τ_s decrease has slowed significantly.) Upon reaching lower saturation, the storage-time recovery process was then observed using an applied bias of polarity opposite to that used to cause degradation.

3.3 RESULTS

Figure 39 shows storage time (τ_s) as a function of time under bias stress at room temperature for MOS capacitors from the Wet N lot. Storage times in upper saturation are in the range 100 to 400 sec. A negative bias stress reduces τ_s to the 1 to 10 msec range for the case of -30V (0.1 to 1 sec for -10V). The time required to reach "lower saturation" is in the range 200 to 1000 min. The right-hand portion of Figure 39 shows that complete recovery of τ_s can be obtained for a positive bias stress. The recovery process usually took about an order of magnitude less time to take place than the degradation process. Data for p-type devices are shown in Figure 40. Note that recovery of the Dry P sample was not complete at the end of the period during which a negative bias stress was applied. Devices from lot KA-09 exhibited only a slight bias-stress effect compared to the results shown in Figure 39 and 40. Negative bias stress for an extended period of time reduced τ_s for these devices by only a factor of two to four. The results for KA-09 are similar in this regard to those obtained by Takino.[10]

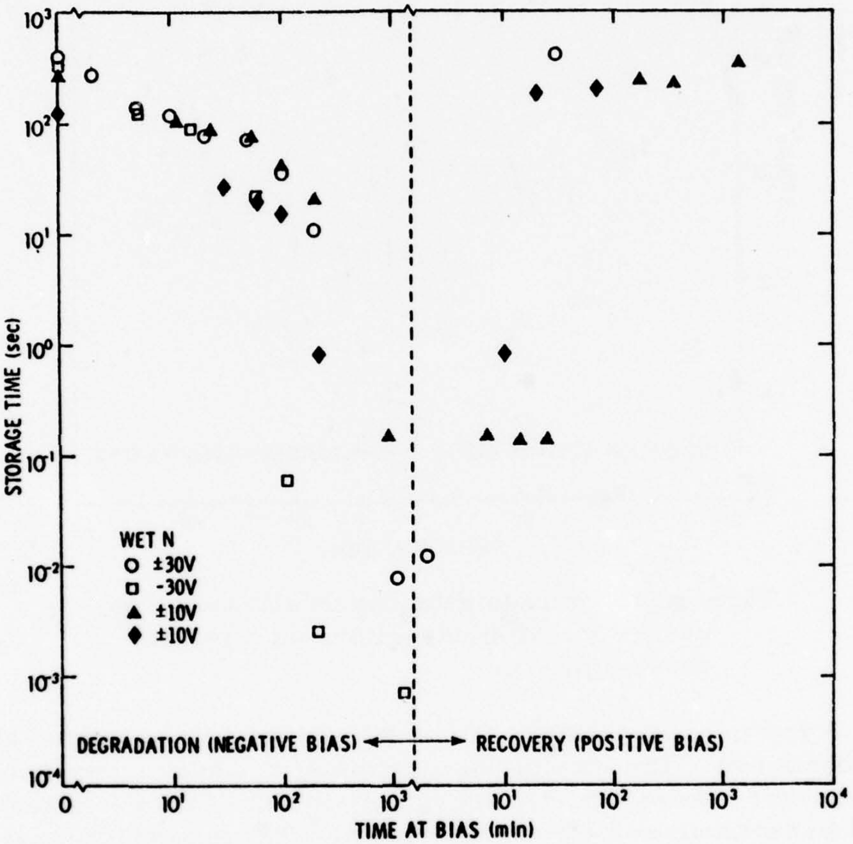

Figure 39. Storage time degradation and recovery for MOS capacitors from the Wet N lot.

---

[10] T. Takino, Ph.D. thesis, UCLA 1976.

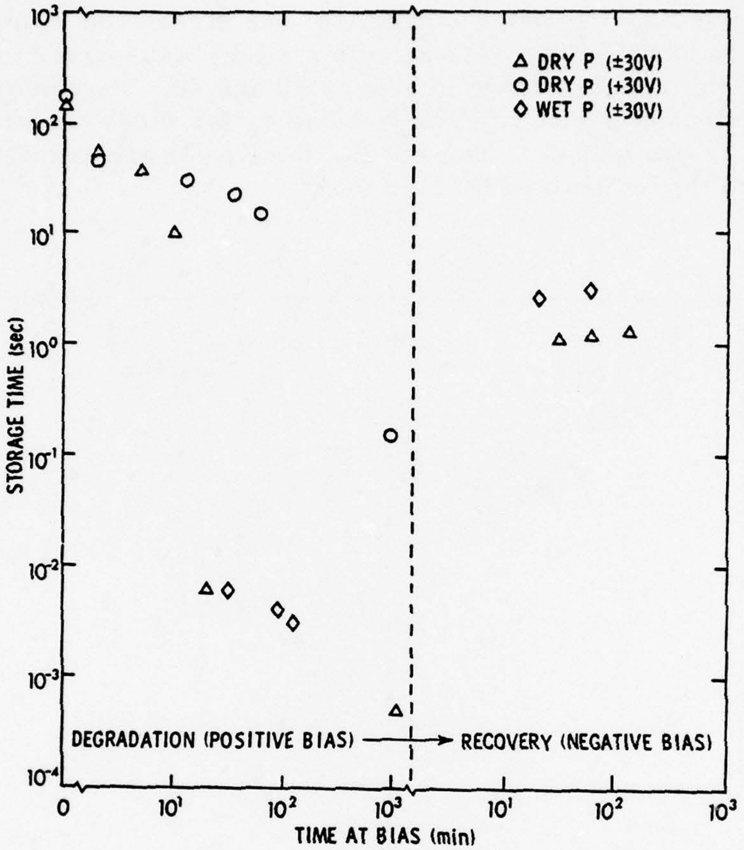

Figure 40. Storage time degradation and recovery for MOS capacitors on a p-type substrate.

A few general features of our bias-stress observations should be mentioned. The rate of degradation of τ_s under inversion-bias stress was observed to depend on the amount of time a device was held in accumulation (upper saturation). The degradation rate was relatively slow for a device previously biased into accumulation for a relatively long time. In addition, the recovery rate was observed to be relatively slow for a device held in lower saturation with an inversion bias for a relative long time. Capacitance versus voltage measurements were also made in upper saturation and in lower saturation. Only a slight shift in flatband voltage (20 to 40 mV) was noted in most cases for both p- and n-type devices.

For n-type devices, the shift was in a positive direction, which is consistent with the movement of positive ions toward the Al electrode since a negative bias stress was applied. For p-type devices, the shift was in a negative direction, which is consistent with the movement of positive ions toward the SiO_2-Si interface since a positive bias stress was applied. It is possible that the observed C-V shifts are due to movement of sodium ions through the oxide.

Figure 41 shows results of Zerbst analysis (described in Section 2.2.2.3) on C-t curves for a Wet N device bias-stressed at -30V.

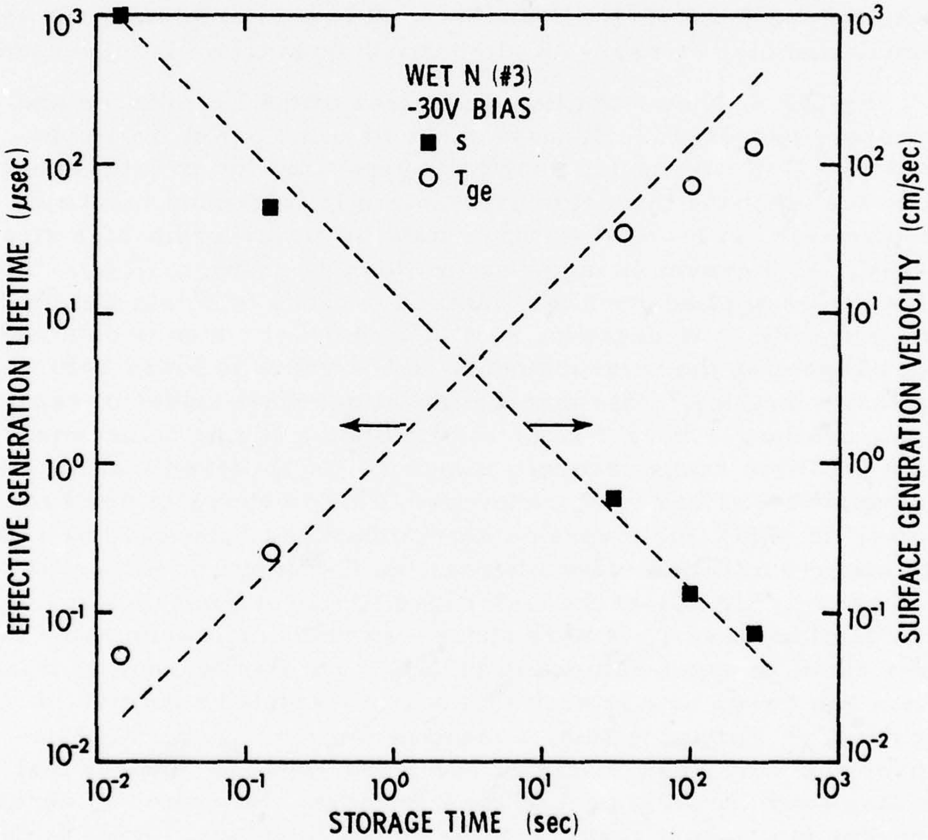

Figure 41. Effective generation lifetime and surface generation velocity as a function of storage time for an MOS capacitor subjected to a negative bias stress. Values of τ_{ge} and s were obtained by Zerbst analysis of C-t curves.

Shown is the effective generation lifetime τ_{ge} and the surface generation velocity as a function of storage time. For long storage times, τ_{ge} is long and is determined by generation at centers in the depletion region bulk (i.e., $\tau_{ge} \rightarrow \tau_g$). As τ_s degrades due to application of a negative bias stress, τ_{ge} also decreases. This is attributable to the increasing importance of carrier generation at centers at the SiO_2-Si interface. The surface generation velocity is observed to increase by orders of magnitude for a comparable change in τ_s and τ_{ge} (Figure 41). Thus, the apparent effect of an inversion bias stress is to temporarily create interface states which enhance the rate of carrier generation, and thereby decrease τ_s. These states can be removed, at least partially and in most cases completely, by an accumulation bias stress. An alternative explanation is discussed below.

Figure 42 shows additional features of the degradation and recovery processes. Illustrated are data for a Wet N sample. In 42(a), C-V curves are shown for upper and lower saturation. It is seen that the inversion capacitance is increased when a device is placed in the lower saturation state by an inversion-bias stress (-10V). C-t curves in upper saturation are shown in 42(b). The bias stress applied for a few hundred seconds to obtain the first trace causes τ_s to degrade, so a different C-t curve is obtained upon repeating the measurement. A C-t curve in lower saturation is shown in 42(c). Note that the initial and final values of capacitance are larger here than in 42(b). Upon applying an accumulation bias (+10V) to cause recovery to occur, we observed that the C-V curve recovers before τ_s recovers. This is shown in 42(d) and 42(e). In 42(d), the inversion capacitance has recovered to near its upper-saturation value whereas the C-t curve in 42(e) still yields a short τ_s. (Note that the C-V curve is flat in inversion in Figure 42(d) because τ_s is very short. At the same sweep rate, the C-V curve in upper saturation (42(a)) is not flat because τ_s is long; i.e., the sweep rate is such that a deep-depleted condition is achieved.) Following this, a process we term "temporary recovery" occurs, as illustrated in Figure 42(f). It appears that τ_s is long from the first part of the C-t curve. However, τ_s abruptly appears to be short again near the end of the trace. After a bias stress on the order of 20 to 100 minutes, "permanent" recovery of τ_s is observed. (Data of the type shown in Figure 42(f) are only observed if the C-t trace is begun in deep depletion instead of inversion.)

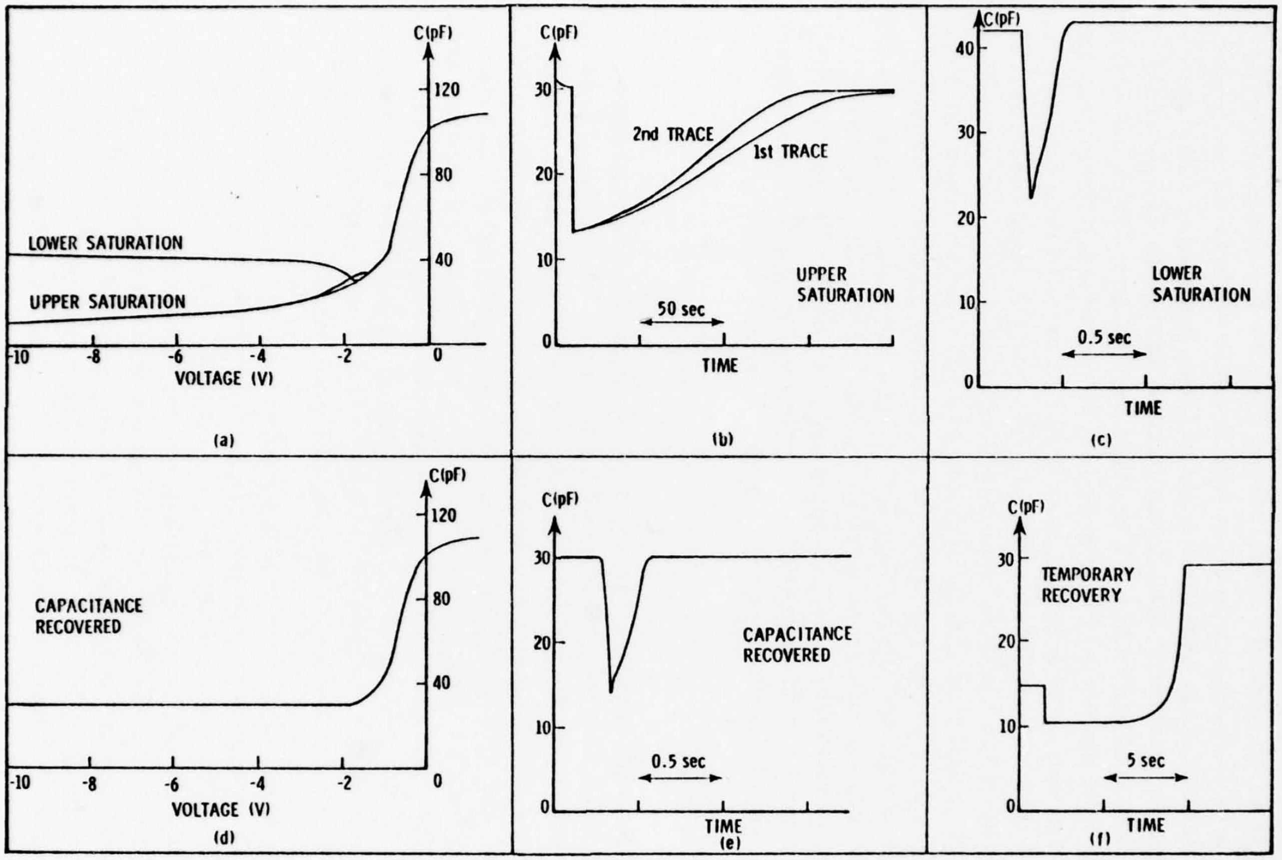

Figure 42. (a) C-V curves in upper and lower saturation for a Wet N MOS capacitor; (b) C-t curves in upper saturation; (c) C-t curve in lower saturation (after -10V bias stress); (d) C-V curve just after application of a recovery bias stress (+10V); (e) C-t curve just after application of a recovery bias stress; (f) C-t curve illustrating the effect on storage time of the inversion bias applied during the C-t measurement. The sweep rate for C-V measurements was 5 V/sec in all cases.

The recovery process depicted in Figure 42(f) was also observed to take on another form, depending on the time following application of a recovery bias at which observations were made. Figure 43 shows data obtained a short time (minutes) after application of +30V recovery bias to an n-type device (a device different from that of Figure 42). The first part of the C-t curve is very similar to that shown in Figure 42(f). However, a second portion is then observed in which the final value of capacitance increases. A trace of this type indicates that τ_s has not yet recovered and also that the capacitance has returned to its lower saturation condition. It should be noted that the temporary recovery phenomena of Figures 42(f) and 43 arise because the accumulation-bias recovery process is perturbed by making a C-t measurement. To make this measurement, an inversion bias is applied to the device which causes degradation to occur once again. Thus, in Figure 42(f) τ_s is initially long but is degraded abruptly during the C-t measurement as a result of the inversion bias.

3.4 DISCUSSION

A qualitative explanation for a portion of the present bias-stress findings can be given based on the work of Takino.[10] However, certain aspects of the data are not yet accounted for, and further work will be required to achieve the needed insight. Takino considered the effect of positive ions in the oxide on the carrier generation rate at interface states. For an n-type substrate, as positive ions approach the interface the electron emission rate decreases. In the p-type case, the approach of positive ions causes the emission rate to increase. These effects are due to the coulombic interaction between the ion and the interface state.[10]

The present C-V data taken in lower and upper saturation are explainable in terms of positive ion motion in the oxide. In addition, if Takino's model is correct, then the C-t (i.e., τ_s) data can also be accounted for qualitatively on the basis of ion motion. In n-type devices, for example, application of a negative-bias stress would move the positive ions away from the interface, thereby increasing the carrier generation rate and decreasing the storage time. A positive-bias stress reverses the process.

---

[10] T. Takino, Ph.D. thesis, UCLA 1976.

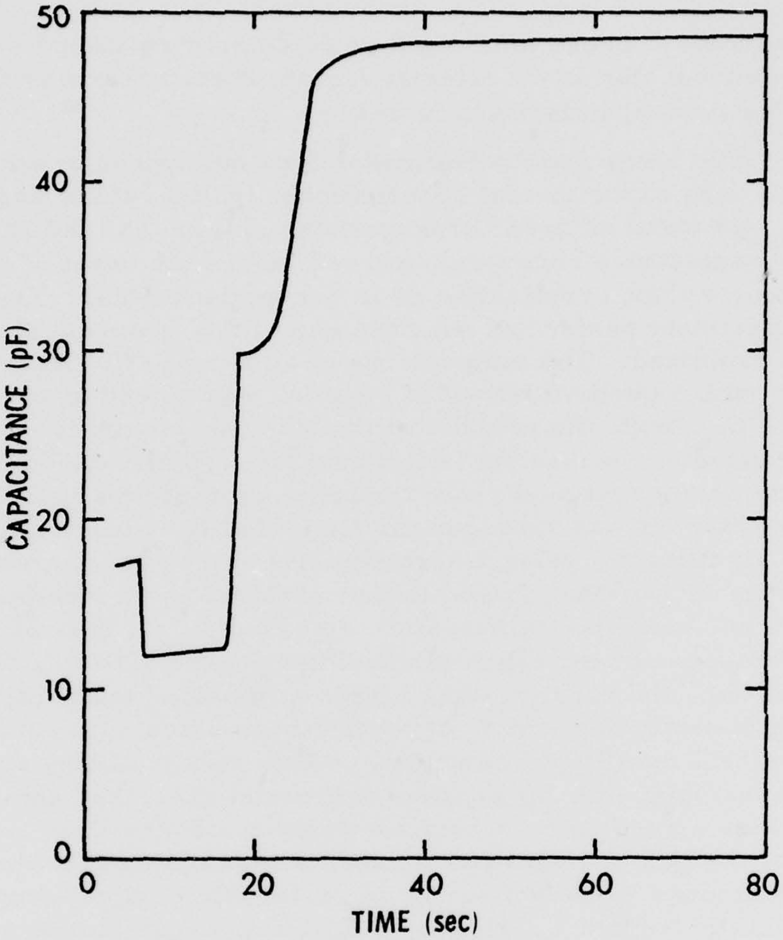

Figure 43. Capacitance versus time for an MOS capacitor illustrating the degradation of τ_s and the increase in inversion capacitance that can occur during a C-t measurement of a device that had a recovery (accumulation) bias applied for a short time (minutes).

The increase in inversion capacitance observed in lower saturation can be accounted for qualitatively in terms of the lateral motion of positive ions. Consider a p-type device as an example. A positive-bias stress drives ions perpendicularly through the oxide to the interface, with a resulting decrease in storage time. The fringing field present gives rise to the laterally depleted region shown in Figure 1. In addition, this fringing field will move ions laterally along the interface beyond the region under the gate electrode. These ions can then deplete an additional portion of the semiconductor in the laterial region, thereby causing the measured inversion capacitance to increase.

The above qualitative model does not appear to account for the following experimental observations: (1) the rate of degradation of τ_s was about an order of magnitude slower than the rate of recovery; (2) capacitance recovery occurred before the onset of storage-time recovery upon application of an accumulation bias. One further experiment performed near the end of this program also needs to be explained. The temperature of an n-type (Wet N) MOS capacitor with a positive bias (30V) applied was raised to either 50 or 100°C. Next, the polarity of the bias was reversed (-30V) and bias-temperature stress then continued for typically one hour. Upon returning the device to room temperature while maintaining the negative bias, it was subsequently found that the time required to degrade τ_s significantly using a negative-bias stress had increased by a factor of 2 to 5 compared to that required in an identical device that had not been bias-temperature stressed (e.g., data of Figure 39). (This experiment was replicated using several Wet N devices.) In addition, the negative-bias stress at elevated temperature did not significantly degrade τ_s at room temperature; i.e., the value of τ_s was still near upper saturation. This recent finding appears to be inconsistent with the positive-ion model described above. However, it does appear to be consistent with our observation, noted above, that the rate of degradation under inversion-bias stress depends on the amount of time a device is previously held in accumulation at room temperature. Holding a device in accumulation at elevated temperature slows the degradation rate much more significantly.

The bias-stress observations reported here are interesting from several viewpoints, including: (1) the potential impact of these effects on the study of MOS device properties; (2) the reliability of MOS devices; (3) the potential relationship between the observed phenomena and interface-state studies at various laboratories (including studies of radiation-induced interface states). Additional study of bias-stress effects are needed before a comprehensive model can be developed. Such a model will be required before the importance of the observed phenomena can be realistically assessed.

SECTION 4.0

LEAKAGE CURRENT PHENOMENA IN IRRADIATED SOS DEVICES*

4.1 INTRODUCTION

Silicon-on-sapphire MOS devices are being developed for radiation-hardened electronic systems because they have several advantages over their MOS-on-bulk-silicon counterparts: reduced transient photoresponse; elimination of latchup; increased packing density and speed. A disadvantage of SOS devices is the occurrence of a significant ionizing-radiation-induced back-channel leakage current in n-channel transistors.[35-37] This phenomenon has been shown to be due to the trapping of positive charge in the sapphire near the silicon-sapphire interface which induces a conducting channel in the silicon.[38,39] We have performed a detailed study of ionizing radiation effects on SOS devices with emphasis placed on determining the mechanisms of back-channel leakage current phenomena.

Several related topics are treated in this section, including: (a) comparison of radiation-induced leakage current for devices with wet and dry gate oxides; (b) radiation-induced reduction of back-channel leakage current; (c) bombarding electron energy dependence of leakage current production and leakage current reduction. This last topic was explored using 6- to 45-keV electrons. The reader's attention is particularly directed to the discussion of radiation-induced reduction of leakage current. This novel mechanism constitutes a potential remedy for leakage current problems in SOS devices employed in a space radiation environment.

---

*Published in the IEEE Transactions on Nuclear Science 24, 2119 (1977).

[35] D. Neamen, W. Shedd, and B. Buchanan, IEEE Trans. Nucl. Sci. 21, 211 (Dec. 1974).

[36] R.A. Kjar and J. Peel, IEEE Trans. Nucl. Sci. 21, 208 (Dec. 1974).

[37] K.M. Schlesier, IEEE Trans. Nucl. Sci. 21, 152 (Dec. 1974).

[38] E. Harari, Appl. Phys. Letters 29, 25 (1976).

[39] E. Harari and D.J. McGreivy, IEEE Trans. Electron Devices 24, 1277 (1977).

4.2 EXPERIMENTAL CONSIDERATIONS

Irradiations were performed at room temperature using the Co^{60} source at Northrop Research and Technology Center and a Jeol JSM-2 scanning electron microscope. The Co^{60} dose rate was 4.3 rads(Si)/s in most cases but in some experiments was increased to 64 rads(Si)/s. Silicon-on-sapphire devices examined in this study were obtained from several sources. Most of the information presented herein resulted from studies on custom n-channel SOS transistors fabricated at Hughes Aircraft (HAC). Sapphire wafers containing a silicon epitaxial layer (initial thickness 0.5 μm) were obtained by Hughes from Union Carbide and devices containing both wet and dry gate oxides were then fabricated. All processing steps were identical for these devices except the gate oxidation. Wet oxides (~980 Å -- pyrogenic) were grown at 925°C whereas the dry-oxide (~930 Å) growth temperature was 1000°C. The gate metallization on most of the transistors was purposely kept thin (750 ±100 Å) to facilitate studies with a low-energy electron beam. Channel width was 8.0 mils and channel length was 0.21 ±0.02 mil. We also investigated radiation-induced leakage current in n-channel transistors contained in radiation-hardened CMOS/SOS inverters obtained from three manufacturers.

Back-channel leakage current I_ℓ was obtained from measurements of drain current versus gate voltage for a constant value of V_{ds}, typically 5V. Such characteristics were recorded on an x-y plotter by applying a ramp voltage to the gate electrode and monitoring drain current by use of a current-to-voltage converter. In addition to obtaining I_ℓ from I_{ds}-V_{gs} characteristics, we also used a circuit to switch momentarily to measurement bias conditions when it was necessary to minimize the time during which irradiation bias conditions were interrupted. A constant I_{ds} (equal to I_ℓ) was achieved only if V_{gs} was several volts negative; conduction along the front channel and at island edges must be turned off before back-channel leakage current alone is observed. Threshold voltage was determined for SOS transistors from measurements of $\sqrt{I_{ds}}$ versus V_{gs} in the conventional way. Front-channel field-effect mobility was also determined from such measurements. In addition, drain characteristics were used to obtain front-channel conductance mobility.

4.3 RESULTS

4.3.1 Threshold Voltage Shifts and Channel Mobility Degradation

Threshold voltage was measured as a function of dose up to 10^7 rads(Si) (Co^{60} -- 64 rads(Si)/s) for dry- and wet-oxide custom transistors. During irradiation and measurement, V_{ds} was equal to 5V, and irradiations were performed with two values of V_{gs}: 0 (grounded gate) and 5V. Both device types were found to be quite radiation tolerant. Under worst-case biasing conditions, the maximum value of threshold voltage shift observed up to 10^7 rads was 1.3V. Interface-state effects were evident (i.e., positive shift in threshold voltage) at high doses for wet-oxide transistors but not for dry-oxide units. McLean et al.[23] previously observed such effects to be more important in wet-oxide devices.

Degradation of front-channel mobility was found to be negligible for dry-oxide transistors after irradiation to 10^7 rads. However, in wet-oxide devices after the same total dose, mobility degraded by roughly a factor of two and this reduction is qualitatively consistent with the interface-state effects noted for such units in threshold voltage measurements. That is, increased scattering is expected when a significant number of interface states have been introduced by radiation.

4.3.2 Leakage Currents in Irradiated Wet- and Dry-Oxide Devices

Figure 44 shows leakage current versus dose for wet- and dry-oxide transistors irradiated using Co^{60} at a dose rate of 4.3 rads (Si)/s. (Discussion of the reduction of I_ℓ shown in the right-hand side of this figure is given in the next subsection.) The irradiation bias values were $V_{gs} = 0$ and $V_{ds} = 5V$. To measure I_ℓ, V_{gs} was switched momentarily to about -7V. Leakage currents for dry-oxide devices are observed to be substantially larger than for their wet counterparts. Behavior is similar in both cases in that plateau regions are evident at high doses and a significant increase in I_ℓ occurs at intermediate doses. (Similar data have previously been obtained by Harari.[38,39]). A slight decrease in leakage current

---

[23] F.B. McLean, H.E. Boesch, Jr., and J.M. McGarrity, IEEE Trans. Nucl. Sci. 23, 1506 (1976).

[38] E. Harari, Appl. Phys. Letters 29, 25 (1976).

[39] E. Harari and D.J. McGreivy, IEEE Trans. Electron Devices 24, 1277 (1977).

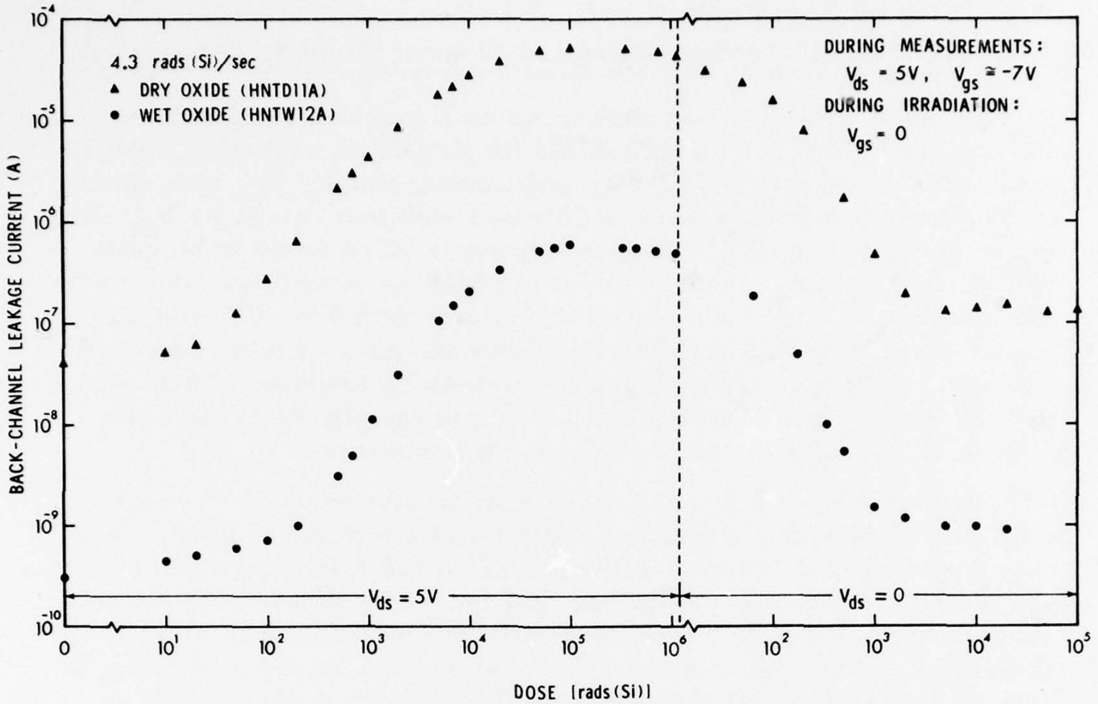

Figure 44. Back-channel leakage current vs dose for dry- and wet-oxide n-channel SOS transistors irradiated with $V_{gs} = 0$ and $V_{ds} = 5V$ at a dose rate of 4.3 rads(Si)/s. The reduction in leakage current in the right-hand portion of this figure was accomplished by continuing to irradiate beyond 10^6 rads with $V_{ds} = V_{gs} = 0$. (Note the change in the dose scale.)

(~20%) is evident as the dose is increased from 10^5 to 10^6 rads. By analogy to effects at the SiO_2-Si interface, this decrease may be due to the introduction of negatively charged states at the Si-Al_2O_3 interface which would compensate for a portion of the positive charge trapped in the sapphire. (For data obtained at a dose rate of 64 rads (Si)/s, this phenomenon was evident but only at about the 5% level.)

At the Northrop Co^{60} facility, a device to be irradiated is placed in the exposure room and the radiation source is then raised up into the room. This takes approximately 5 minutes, during which time the dose rate is time varying. A maximum rate is reached when the Co^{60} source is completely raised. As discussed below, it was found that a small photocurrent dominated behavior shown in Figure 44 for the wet-oxide device for doses up to 200 rads (the approximate dose received during raising of the Co^{60} source for the case of a maximum rate of 4.3 rads(Si)/s). This current scaled with dose rate and served to mask true back-channel behavior at low doses. To examine only the radiation-induced back-channel leakage component of measured current, both the photocurrent and the pre-irradiation current were subtracted from measured values.

Figure 45 shows radiation-induced back-channel leakage current versus dose based on data in Figure 44. The large vertical error bar for the lowest-dose wet-oxide data point reflects primarily the accuracy of the photocurrent correction made at that dose. Also shown in Figure 45 (solid circles) is a horizontal translation of

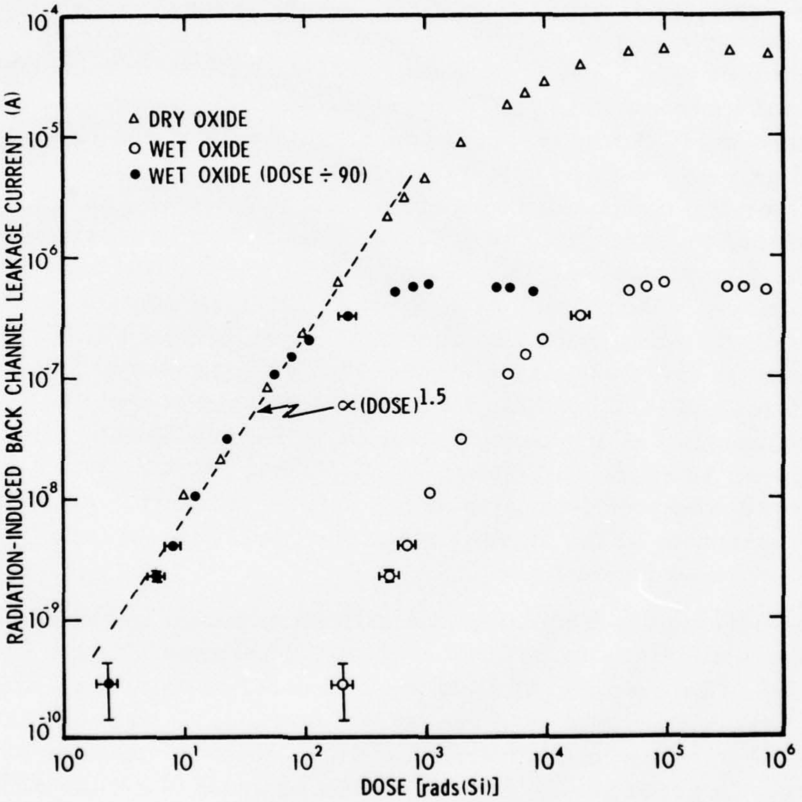

Figure 45. Radiation-induced leakage current vs dose for wet- and dry-oxide SOS transistors irradiated at a rate of 4.3 rads (Si)/s. These data were obtained by correcting the data of Figure 44 for pre-irradiation current and, in the wet-oxide case, for a photocurrent component.

wet-oxide data by a factor of 90 in dose. This translation illustrates that both wet and dry data can be described by the same power law (current $\propto$ (dose)$^{1.5}$) over approximately three orders of magnitude variation in radiation-induced leakage current. If we consider wet and dry data separately, the (dose)$^{1.5}$ dependence in the wet case is observed over a leakage current range of approximately two orders of magnitude for doses between 500 and 10^4 rads(Si). For dry devices, this dependence is also noted over approximately two orders of magnitude variation in current for doses between 20 and 500 rads.

Before interpreting the results of Figure 45, it is useful to consider the temperature dependence data of Figure 46. Shown is leakage current versus 1000/T for wet- and dry-oxide transistors before and after irradiation to several doses. Before irradiation, data for wet devices exhibit two regimes with activation energies differing by a factor ot two. The high-temperature regime is most likely due to thermal generation in the drain depletion region. For a single generation level at mid-gap, the dominant term in the expression for thermal generation rate will be n_i, the intrinsic carrier concentration. Over the temperature range of interest, n_i is approximately proportional to exp(-0.60 eV/kT) and thus the 0.57 eV slope in Figure 46 is consistent with the domination of generation current at high temperatures. Harari and McGreivy[39] obtained convincing evidence that pre-irradiation leakage current at room temperature in wet-oxide devices very similar to those studied here is attributable to thermal generation. Although the present results are consistent with their findings, it is interesting to note in Figure 46 that this statement only applies at room temperature and above. At lower temperatures for unirradiated wet devices and for both device types under all other conditions shown in the figure, measured leakage current is dominated by back-channel phenomena.

Formation of a channel in the silicon adjacent to the Si-Al_2O_3 interface occurs due to buildup of positive trapped charge N_t^+ in the sapphire. The quantity N_t^+ induces a carrier density n_{inv} and the resulting leakage current is given by $e F A n_{inv} \mu_{bc}$, where F is applied field, A is cross-sectional area, and μ_{bc} is back-channel carrier mobility. In general, N_t^+ and n_{inv} will be related nonlinearly. Additionally, μ_{bc} is expected to vary with n_{inv}. Work of Brews,[40]

---

[39] E. Harari and D.J. McGreivy, IEEE Trans. Electron Devices 24, 1277 (1977).

[40] J.R. Brews, J. Appl. Phys. 46, 2181 (1975); 46, 2193 (1975).

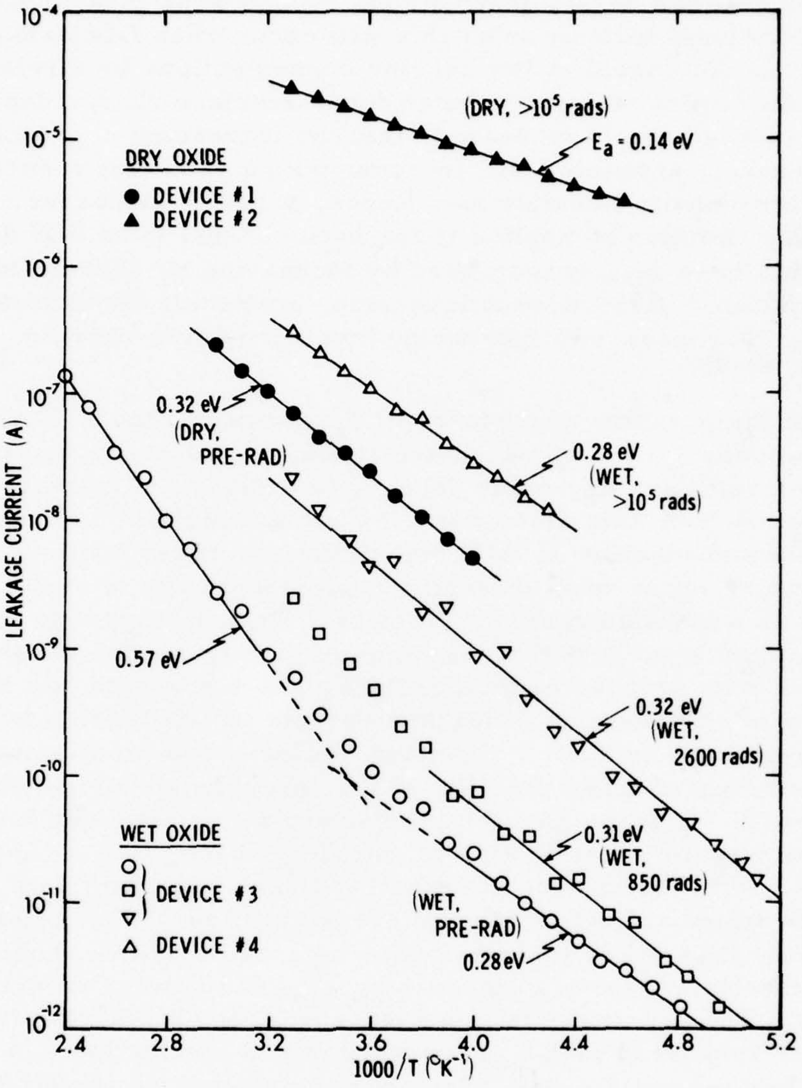

Figure 46. Leakage current vs reciprocal temperature for wet- and dry-oxide SOS transistors. Data obtained before irradiation and after irradiation to several values of total dose are shown.

Chen and Muller,[41] and Guzev et al.[42] has revealed that front-channel mobility in an MOS transistor in weak inversion is constant for very low values of n_{inv} ($\leqslant 10^9$ cm^{-2}) and increases with n_{inv} for higher values of this quantity (but still in weak inversion). Brews' analysis indicates that this will occur when front-channel mobility is dominated at low carrier concentrations by a relatively high, inhomogeneously distributed fixed interface charge density. As the gate voltage is increased, thereby increasing n_{inv} in the front channel, screening will increase with a resultant reduction in carrier-density fluctuations. Hence, mobility increases. (This reasoning can also be applied to the back channel in an SOS device but in this case n_{inv} is increased by increasing N_t^+ through ionizing radiation.) Beyond weak inversion, scattering dominates and mobility decreases with increasing inversion-layer carrier density.[40-42]

The temperature dependence of I_ℓ shown in Figure 46 yields activation energies (E_a) which are roughly equal except for the case of post-irradiation dry-oxide data. (We exclude the thermal generation regime from this discussion.) Chen and Muller[41] observed that front-channel mobility in MOS transistors decreased with decreasing temperature in the weak inversion regime and plots of such data yielded an activation energy of ~0.1 eV. Data in Figure 46 are qualitatively consistent with their findings in that I_ℓ is also observed to decrease with decreasing temperature, which suggests that the temperature dependence of leakage current is attributable to that of back-channel mobility. Chen and Muller proposed a temperature-activated front-channel mobility at low inversion-layer carrier densities, with E_a being an effective barrier associated with a non-uniform potential distribution at the SiO_2-Si interface. (Analysis by Brews[40] indicates that interpreting channel mobility data in terms of temperature activation may be oversimplified.) This effective barrier is lowered by an increase in n_{inv} and thus one should observe an E_a that decreases with increasing n_{inv} in the weak inversion regime. The dry-oxide data in Figure 46 are qualitatively consistent with this concept in that E_a decreased due to irradiation (i.e., higher back-channel n_{inv}). The observation that wet-oxide devices

---

[40] J.R. Brews, J. Appl. Phys. 46, 2181 (1975); 46, 2193 (1975).

[41] J.T.C. Chen and R.S. Muller, J. Appl. Phys. 45, 828 (1974).

[42] A.A. Guzev, G.L. Kurishev, and S.P. Sinitsa, Phys. Status Solidi A14, 41 (1972).

yielded approximately the same value of E_a under all conditions shown in this figure is qualitatively consistent with the front-channel data of Chen and Muller, where, at a given temperature, mobility (and thus E_a) was observed to be nearly constant in very weak inversion for several temperatures near 300 K.

Pre-irradiation data in Figure 46 for the dry-oxide device are very similar to post-irradiation wet-oxide findings. This suggests that a back channel already exists in dry devices before irradiation, whereas in the wet case pre-irradiation leakage current at room temperature is dominated by thermal generation in the drain depletion region. Harari and McGreivy[39] have explained such behavior in terms of the existence of a processing-produced n-type layer in the silicon adjacent to the Si-Al_2O_3 interface for dry-oxide devices. They ruled out trapped charge in the Al_2O_3 as being responsible for pre-irradiation leakage current in such devices because they were unable to reduce I_ℓ by optical excitation.

Interpretation of the room-temperature data of Figure 45 is now given. The same functional dependence of radiation-induced leakage current on ionizing dose is exhibited for wet- and dry-oxide devices, which suggests that the same physical processes are occurring in both cases. The factor-of-ninety displacement in dose exhibited in the figure (i.e., a larger dose required to achieve a given value of I_ℓ in wet devices) then needs to be accounted for. At some constant value of radiation-induced leakage current, the product of mobility and carrier density in the back channel for the dry-oxide case must be equal to that for wet oxide. Such a comparison can be made for leakage currents ranging from $\sim 10^{-8}$ to $\sim 3 \times 10^{-7}$ A and for doses ranging from ~10 to ~200 rads for dry oxide and from $\sim 10^3$ to $\sim 2 \times 10^4$ rads for wet oxide. Since the rate at which the mobility-carrier density product increases with dose is the same for wet and dry devices, one is tempted to conclude that at a given value of leakage current mobilities are equal and carrier densities are equal for the two transistor types. The displacement in dose exhibited in Figure 45 would then be attributed to a larger density of traps in dry-oxide devices than in their wet-oxide counterparts. The fact that leakage-current saturation occurs at approximately the same dose suggests that the same trap is responsible for observed behavior in both cases.

---

[39] E. Harari and D.J. McGreivy, IEEE Trans. Electron Devices 24, 1277 (1977).

Acceptance of a significantly larger trap density in dry-oxide devices then suggests that in the wet case only a very small fraction of the holes generated in the Al_2O_3 per unit dose are trapped there.

An alternative to the above explanation is that identical traps and trap densities exist in the sapphire for wet and dry devices. Data of Figure 45 could then be explained in terms of a higher mobility in dry-oxide devices than in their wet counterparts. For equal trapped charge densities, it seems reasonable to assume that n_{inv} would be comparable for the two device types. However, this would then require that μ_{bc}(dry) be a factor on the order of 10^3 larger than μ_{bc}(wet) in the nonsaturation regime and about two orders of magnitude larger in saturation. This requirement seems unreasonable and we judge this alternative explanation to be much less attractive than the unequal-trap-density model suggested above.

The data of Figure 45 cannot be explained simply on the basis of differing silicon doping conditions. As mentioned above, the presence of an n-type layer in dry devices can account for the large <u>pre-irradiation</u> value of I_ℓ compared to that in wet units. If we assume equal trap densities, equal trapped charge densities at a given dose, equal back-channel mobilities at a given n_{inv}, and unequal silicon doping conditions in the two cases, an initial difference in I_ℓ versus dose behavior is expected, similar to that shown in Figure 45 at low doses. However, at higher doses where leakage currents are significantly larger than pre-irradiation values, data for wet-oxide devices would merge with dry-oxide data and the saturation value of I_ℓ would be the same in both cases. Since behavior of that nature is not observed, we therefore rule out such an explanation.

In order to determine the dry-to-wet trap-density ratio responsible for the factor-of-ninety displacement in Figure 45, one would need to relate N_t^+ (or dose) quantitatively to n_{inv} or μ_{bc}. The present data do not yield these relations. It is interesting to note that the dry-to-wet I_ℓ ratio in saturation is also 90. However, this is fortuitous since, as shown in Figure 46 (devices 2 and 4), the saturation ratio varies with temperature due to the temperature dependence of μ_{bc}. On the other hand, the <u>displacement</u> ratio is expected to be temperature invariant since it depends only on the trap-density ratio under the present interpretation.

4.3.3 Radiation-Induced Reduction of Back-Channel Leakage Current

The right portion of Figure 44 illustrates the phenomenon of radiation-induced reduction of back-channel leakage current. Reducing V_{ds} to zero after radiation-induced increases in I_ℓ have been observed caused I_ℓ to decrease dramatically to near its pre-irradiation value if irradiation is continued in this bias condition. To obtain the recovery data of Figure 44 (note break in dose axis just beyond 10^6 rads), V_{ds} was reduced to zero after 10^6 rads and irradiation continued. To measure leakage current at a given dose, V_{ds} was momentarily switched to 5V and V_{gs} to -7V (typically). This measurement took 2 to 3 sec and then V_{gs} and V_{ds} were returned to zero. If the measurement is not made rapidly, then I_ℓ will increase significantly during the measurement period. It is seen that a few thousand rads is sufficient to reduce I_ℓ to a saturation level.

The I_ℓ reduction process can be repeated as evidenced by data in Figure 47. This figure shows findings for a wet-oxide transistor irradiated with $V_{ds} = 5V$ to a dose of 10^3 rads, at which point V_{ds} was reduced to zero and irradiation continued. Substantial recovery is evident. This process was repeated for four more cycles as shown. Upon completion of this cyclying experiment, the Co^{60} source was lowered (dose rate = 0), with a resulting decrease in I_ℓ to within 25% of the pre-irradiation value. The Co^{60} source was raised again (with $V_{ds} = 0$) and I_ℓ increased, and we attribute this increase to a photocurrent. (In Figure 44, the final value of I_ℓ for the wet device following radiation-induced recovery was influenced by the photocurrent and subtracting it reduces measured I_ℓ to within 50% of its pre-irradiation value.) The recovery phenomenon observed here suggests that periodic reduction of V_{ds} to zero to cause a reduction in I_ℓ is a potential remedy for leakage current problems in SOS devices employed in a space radiation environment.

Leakage current studies were made on n-channel transistors contained in CMOS/SOS inverters from three manufacturers to determine whether the radiation-induced I_ℓ reduction process observed for custom transistors (Figures 44 and 47) was general. Large variations in radiation response were observed from lot to lot for inverters. However, the recovery phenomenon was evident for all devices examined. It is interesting to note that in several

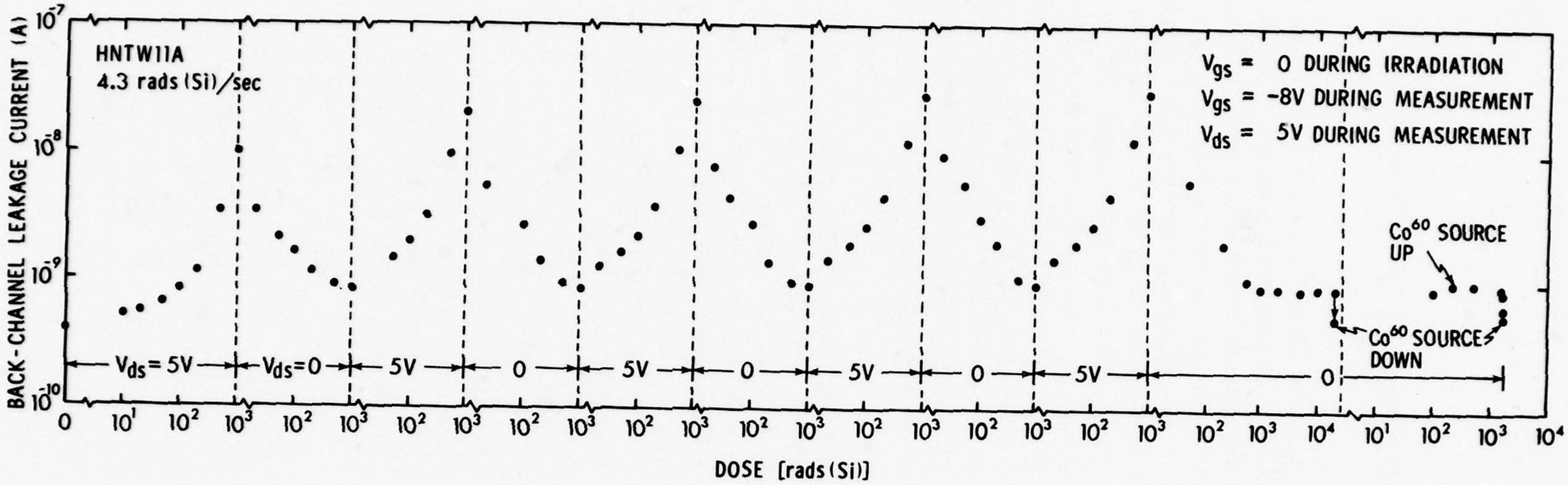

Figure 47. Leakage current vs dose for a wet-oxide SOS transistor irradiated using Co^{60}. The effect of irradiating with V_{ds} = 5V and V_{ds} = 0 is illustrated. (Note changes in dose scale.)

cases the final value of I_ℓ following leakage current production and subsequent radiation-induced reduction was actually less than the pre-irradiation value. In one case, post-recovery I_ℓ was an order of magnitude smaller than prior to bombardment.

4.3.4 Scanning-Electron-Microscope Studies of Leakage Current Production and Reduction

Experiments were performed using a scanning electron microscope (SEM) as a source of localized, nonpenetrating ionizing radiation for the purpose of gaining understanding of the mechanisms of leakage current production and reduction in irradiated SOS devices. Energy deposition profiles for low-energy electrons incident on low-Z materials can be calculated based on the work of Everhart and Hoff[43] and Figures 48 and 49 show profiles appropriate for the geometry of the present custom transistors (thin gate metallization). In Figure 48, profiles for energies from 6 to 16 keV are shown and, for convenience, effective thicknesses of Al, Si, and Al_2O_3 are given based on density ratios relative to SiO_2. It is seen that significant energy deposition occurs in the sapphire for energies $\geqslant 9$ keV. Figure 49 shows deposition profiles at higher energies and only the sapphire portion of a transistor is shown. For this figure, distances shown correspond to actual distances into the sapphire. (In discussion below, the term "electron range" in the Al_2O_3 is used and this refers here to that distance at which $dE/dx = 0$ in Figure 49.)

Irradiations were performed by raster scanning the beam over a device for an integral number of scans. Beam current was measured by means of a Faraday cup which was mechanically moved into position between irradiations of a device. The beam current was reduced to the range of 1 to 6 pA by means of intensity modulation at 50 kHz using a combination of ac and dc deflection of the beam. Uniformity of irradiation over a device is assured by use of a defocused beam. In spite of the use of low beam current and a defocused beam, a significant difference between Co^{60} and SEM irradiation conditions is the much higher dose rate in the latter case. In the present study, the dose-rate ratio exceeded 10^4 in most cases. Operation was restricted to a beam current range where dose-rate effects on measured leakage current were observed to be relatively small.

---

[43] T.E. Everhart and P.H. Hoff, J. Appl. Phys. 42, 5837 (1971).

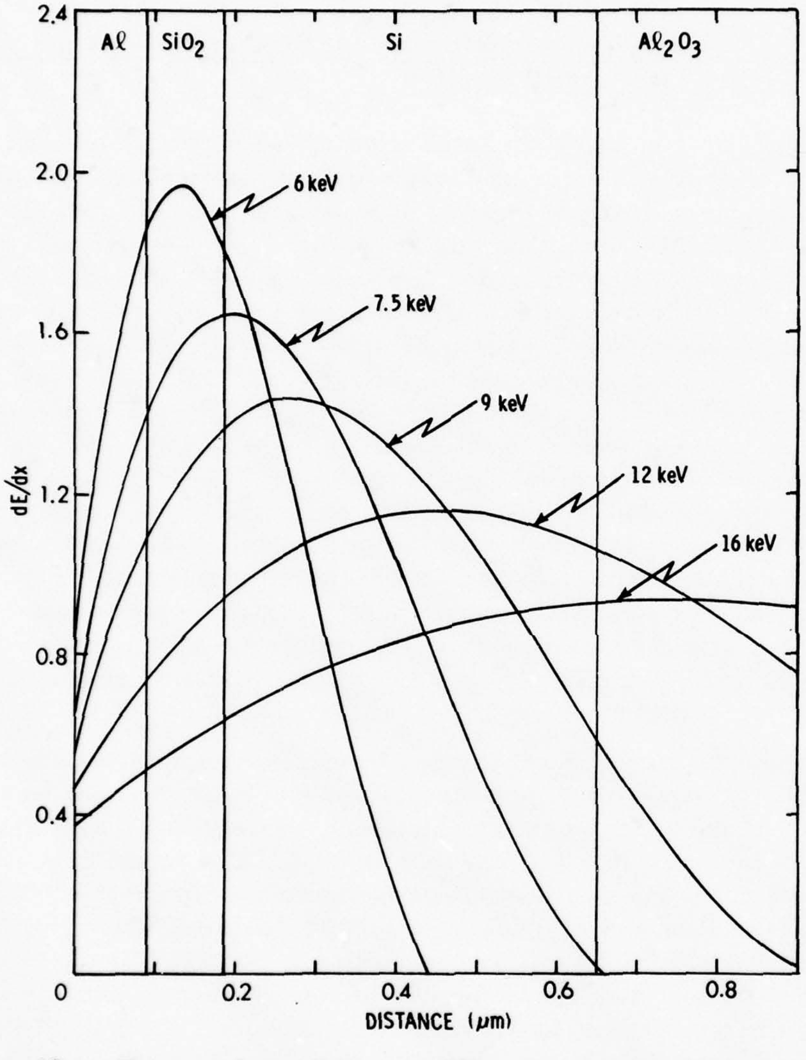

Figure 48. Energy deposition profiles for custom SOS transistors bombarded by low-energy electrons. Profiles were calculated using the work of Everhart and Hoff [43] and effective thicknesses of Al, Si, and Al_2O_3 are shown based on density ratios relative to SiO_2.

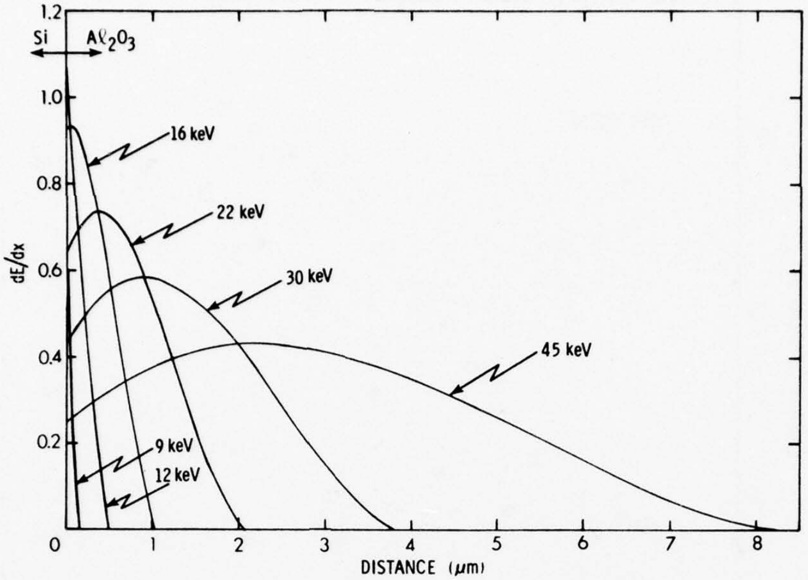

Figure 49. Energy deposition profiles for the sapphire substrate of custom SOS transistors bombarded by low-energy electrons. In contrast to **Figure 48,** the x axis corresponds to actual distances into the sapphire. Note that the Si-Al_2O_3 interface is coincident with the y axis.

Leakage current studies using the SEM were performed on one dry-oxide chip and one wet-oxide chip, each of which contained several transistors. The most complete set of data were obtained for two wet-oxide devices connected in parallel and irradiated simultaneously, and we therefore concentrate on these results here. Results for dry-oxide devices were in qualitative agreement with wet-oxide findings over the energy range for which comparable data were obtained (8 to 18 keV). It is significant to note that the process of radiation-induced reduction of leakage current permits the performance of various radiation effects experiments on a given device since the device can be returned to near its original condition by simple irradiating with $V_{ds} = 0$. This procedure was followed here.

In one series of experiments on wet-oxide transistors, the effectiveness of bombarding electrons of various energies in giving rise to back-channel leakage current was examined. **Figure 50** shows leakage current versus total energy incident on the gate electrode for

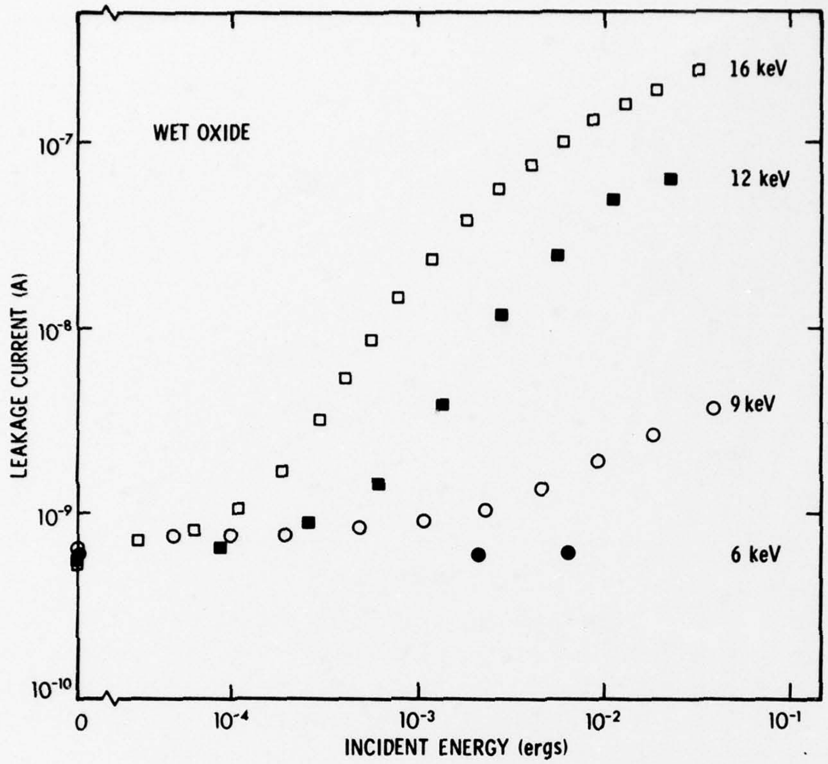

Figure 50. Leakage current vs energy incident on the gate electrode of a wet-oxide SOS transistor. Data for several bombarding electron beam energies are shown.

four beam energies, ranging from 6 to 16 keV. These data are presented in terms of total incident energy since, as is evident in Figure 48, nonuniform energy deposition in four materials is involved and it is difficult to establish a more meaningful base for comparison. It is seen that 6-keV electrons do not cause an increase in leakage current whereas the higher-energy cases do. Upon comparing the results of Figure 50 with the profiles of Figures 48 and 49, the following conclusion becomes evident: Energy must be deposited in the sapphire before radiation-induced increases in back-channel leakage current will be observed. For the 6-keV case, the energy deposition profile peaks in the SiO_2 and the maximum dose deposited in the layer was ~3 x 10^5 rads(Si). At 16-keV, the peak of the profile was just within the sapphire and a relatively high rate of leakage current production is observed.

Figure 51 presents radiation-induced back-channel leakage current versus dose for bombardment with 30- and 45-keV electrons. For reasons which are discussed below, dose in both cases was obtained using the average value of the energy-deposition-profile amplitude over the first 2 μm of the sapphire. Shown for comparison are Co^{60} data for a wet-oxide transistor taken from Figure 45. The 30-keV data are in agreement with 45-keV findings and a general similarity exists between Co^{60} and electron data. Saturation values of I_ℓ observed at high doses are quite similar and the rates of leakage current production are at least comparable. The results illustrated in Figure 51 lead us to a second conclusion: Energy deposition in the bulk of the sapphire (i.e., at distances greater than several μm from the Si-Al_2O_3 interface) is unimportant in terms of giving rise to back-channel leakage current. This point is clearly illustrated by considering the 30-keV profile of Figure 49. Electrons of this

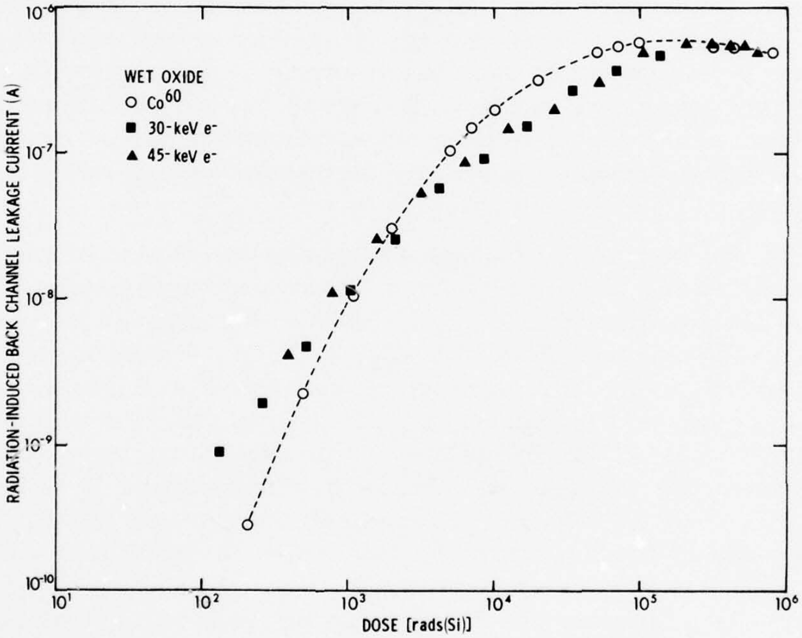

Figure 51. Radiation-induced back-channel leakage current vs dose for wet-oxide SOS transistors. The Co^{60} data shown are from Figure 45. For electron bombardment, the dose shown corresponds to the average energy deposited in the first 2 μm of the sapphire substrate.

energy only penetrate a few μm into the sapphire but give rise to a saturation I_ℓ nearly equal to that produced by Co^{60} gamma rays which penetrate through the entire sapphire thickness (several hundred μm).

Further insight regarding leakage current production is gained by considering the electron energy dependence of saturation leakage current as shown in **Figure 52.** This figure presents saturation values as a function of electron range in the sapphire. (Shown for comparison is the mean value obtained from Co^{60} measurements on a set of transistors from the same lot.) These results suggest a model in which the relevant hole traps are distributed to a depth of several μm within the sapphire, where only a fraction of these traps can be populated at lower beam energies. However, the alternative hypothesis, in which the traps are located at the Si-Al_2O_3 interface (just inside the Al_2O_3), cannot be ruled out by these data because, as discussed below, neutralization of trapped charge occurs simultaneously with the production process. These two processes have different beam energy dependences and come into equilibrium in saturation at each beam energy. A fit based on these competing processes is shown in **Figure 52**, which demonstrates, as will be seen, that the observed saturation behavior can be explained without invoking spatially distributed traps within the sapphire.

For the purpose of further examining the region of importance in the sapphire, the effectiveness of various beam energies in giving rise to leakage current was considered. We define a relative production effectiveness (RPE) as $\Delta I_\ell / E_b \int I_b \, dt$, where E_b and I_b are beam energy and beam current, respectively, and ΔI_ℓ is the change in leakage current produced by a given total incident energy. Figure 53 presents RPE versus electron beam energy (open circles) for a wet-oxide transistor. A peak in effectiveness is observed in the range 16 to 18 keV, corresponding to beam energies at which the deposition profile peaks at some slight distance into the sapphire. The sharp decrease in RPE evident in **Figure 53** at low beam energies is primarily due to the smaller fraction of total incident energy which reaches the sapphire. The decrease in RPE evident at higher beam energies is consistent with either of the following interpretations: (1) a finite spatial distribution of traps which are effective in increasing I_ℓ extends into the sapphire a distance on the order of 2 μm, or (2) an effective generation region (or collection volume) extends ~2 μm into the Al_2O_3. In the latter case,

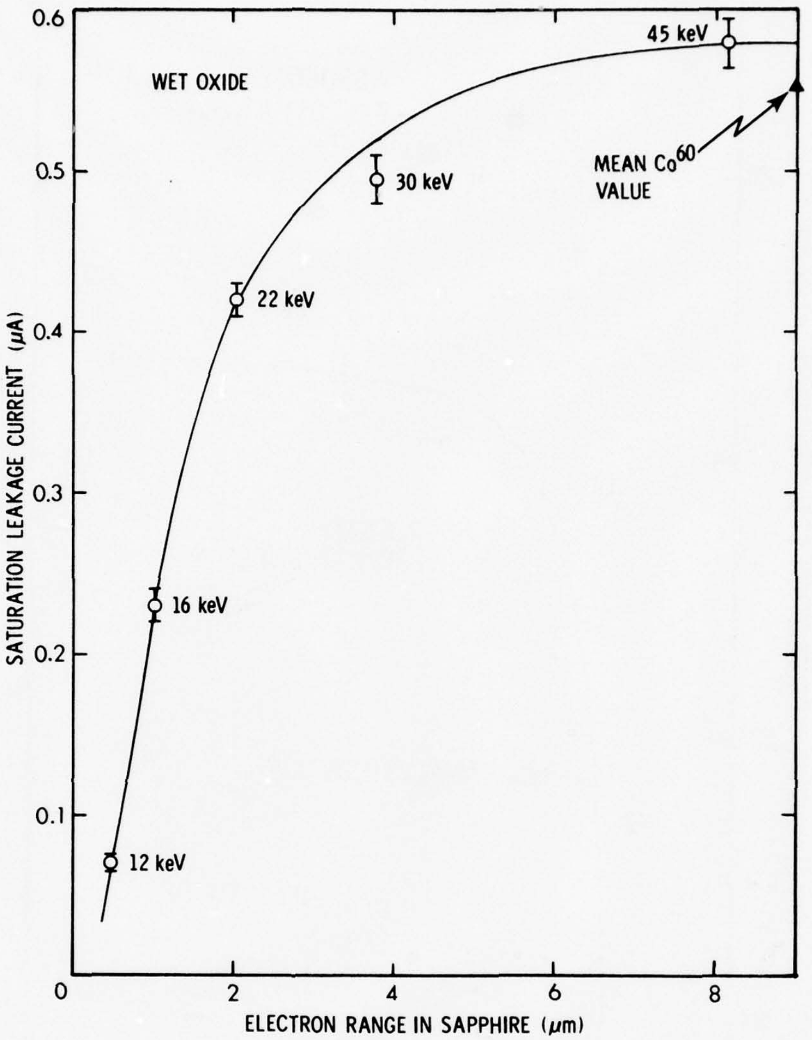

Figure 52. Saturation leakage current vs electron range in sapphire for a wet-oxide SOS transistor irradiated with electrons of various energies. The mean Co^{60} saturation value (averaged over several samples) is also shown for comparison. The electron ranges shown correspond to distances at which dE/dx = 0 in Figure 48. The analytical fit is based on simultaneous production and reduction processes (see text).

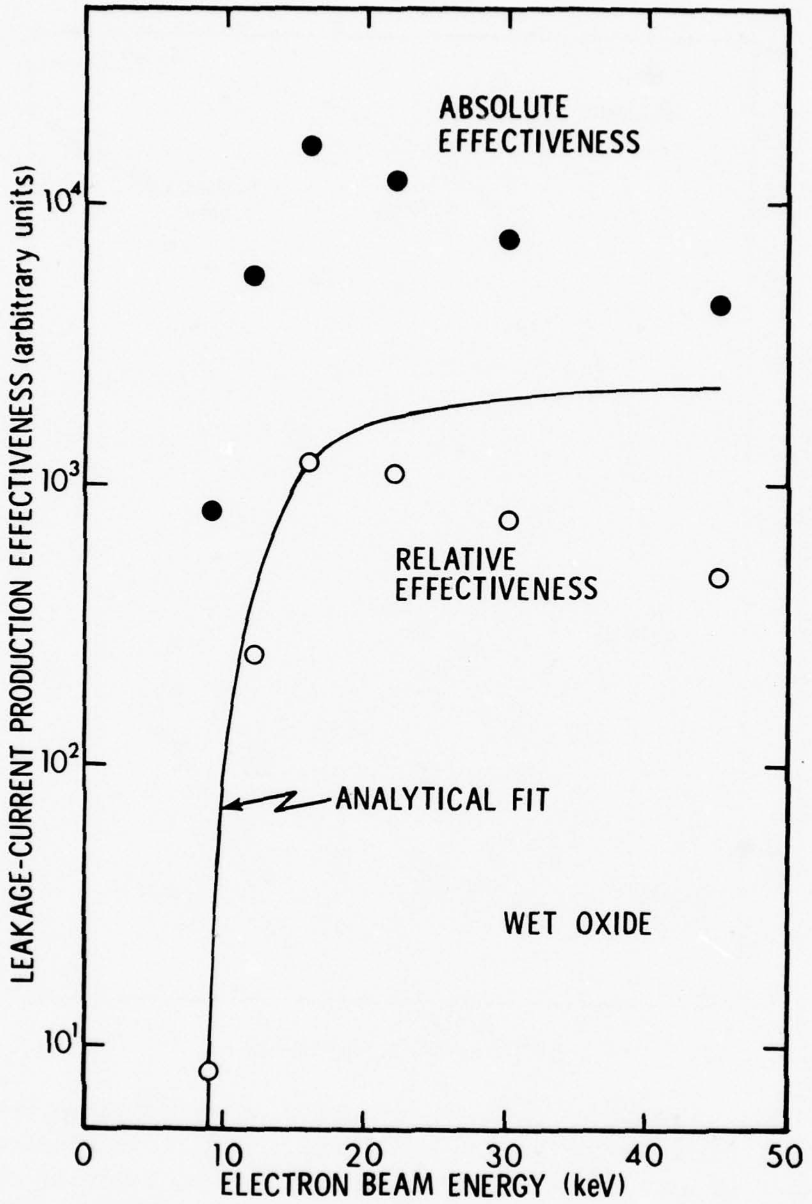

Figure 53. Leakage-current production effectiveness vs electron beam energy for an irradiated wet-oxide SOS transistor. The fit shown is based on simultaneous production and reduction processes (see text).

generated holes would drift to traps located at the Si-Al_2O_3 interface. The important point to note is that the first few µm of the sapphire are shown here to be important in the leakage current production process. It was on this basis that we chose to express dose for the 30- and 45-keV data in Figure 51 in terms of energy deposited in the first two µm.

Since energy deposited in the sapphire is the important quantity in terms of leakage current production, it should be meaningful to express RPE in absolute terms by multiplying the denominator of the RPE expression by that fraction f(E) of incident energy which is deposited in the sapphire. (The upper curve in Figure 54 shows f(E) versus electron beam energy.) Absolute production effectiveness (APE), determined in this manner, is shown in Figure 53. The dropoff in effectiveness at low beam energies was unexpected since the APE should be independent of energy at low beam energies if f(E) is the governing quantity. Several factors could be responsible for observed behavior. Experimental uncertainties are considerably larger for the low-energy data points due to the extreme sensitivity of f(E) at such energies to assumed silicon thickness. Additionally, production effectiveness had to be evaluated differently at 9 keV than in higher energy cases since a comparable range in leakage current was not covered (i.e., ΔI_ℓ was different). In view of the nonlinear dependence of I_ℓ on dose, this implies an additional uncertainty in the 9-keV case. The above-mentioned competition between production and reduction processes may also be present, however, and would yield a dropoff in production effectiveness at low beam energies. A fit to the RPE curve based on such a model is shown (discussed further below). The fit does not take into account the finite range of the production process, and thus correspondence with data at high beam energies is not expected.

Studies of leakage current reduction were performed as a function of bombarding electron beam energy, and Figure 54 shows reduction effectiveness versus energy (open circles) for a wet-oxide transistor. Reduction effectiveness is defined similarly to production effectiveness in that it is a measure of the total incident energy required to reduce I_ℓ by a certain (constant) amount. The experimental procedure at a given beam energy was to increase I_ℓ by bombardment with V_{ds} = 5V and then to decrease I_ℓ by zero-bias irradiation. As in the case of production effectiveness (Figure 53), reduction effectiveness peaks at an intermediate energy, in this case about 11 to 12 keV. However, the decrease in reduction effectiveness at higher beam energies is much stronger than in the

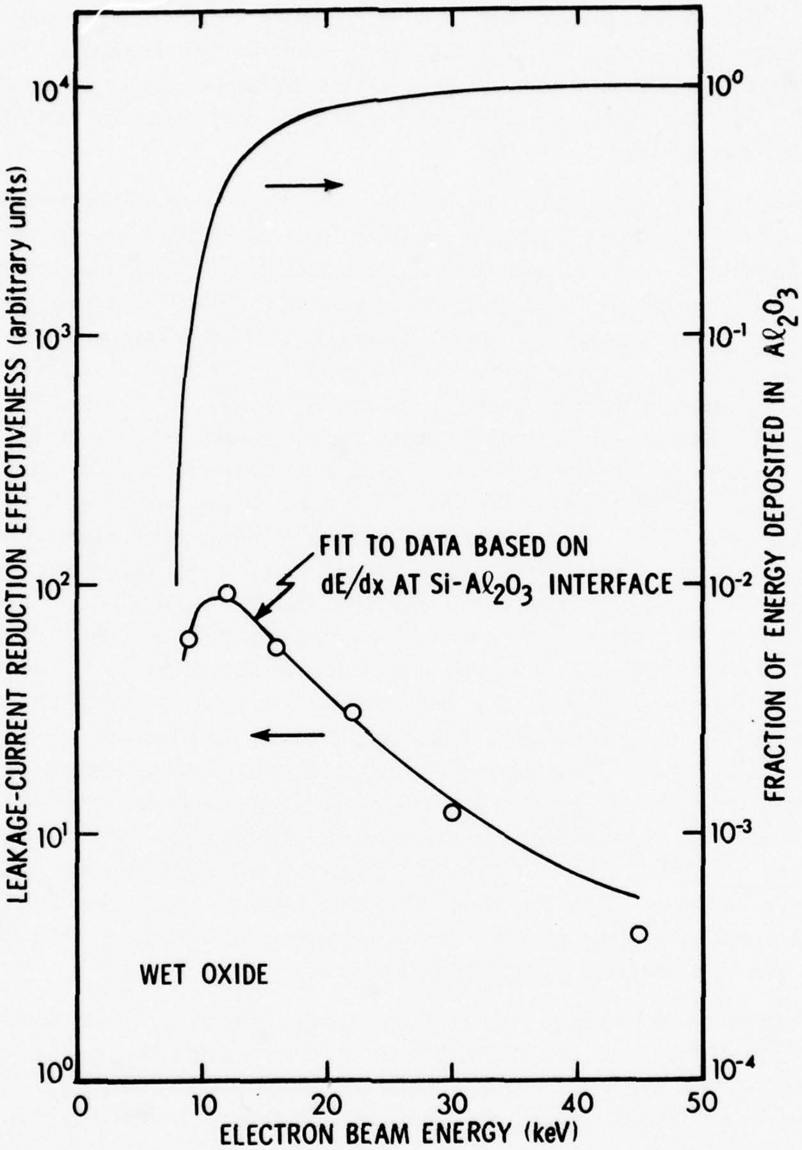

Figure 54. Leakage-current reduction effectiveness (left scale) vs bombarding electron beam energy for a wet-oxide SOS transistor. A fit to the data based on the amplitude of the energy deposition profile at the Si-Al_2O_3 interface is shown. Also shown (upper curve, right side) is the fraction of energy deposited in Al_2O_3 based on the profiles of Figures 48 and 49.

production case which suggests that energy deposition in the sapphire is not the governing parameter in the reduction process. On the other hand, an excellent fit to the data is obtained using the amplitude of the energy deposition profile at the Si-Al_2O_3 interface. This suggests that electron injection into the sapphire is the dominant leakage current reduction mechanism. If traps are distributed within the sapphire, that conclusion is inescapable. If, however, traps are located at the interface, the above finding does not rule out radiation-induced depopulation as a contributing mechanism.

Having described the energy dependence of the reduction process, we now return to consideration of the energy dependence of saturation leakage current and relative production effectiveness (Figures 52 and 53). Whereas with zero bias only the reduction process is operative, under bias both the production and reduction processes occur simultaneously, the latter coming into play as saturation is approached. If the former is governed by f(E) and the latter by dE/dx (evaluated at the interface), then both saturation leakage current and production effectiveness should be described by an appropriate weighting of these two terms. The fits in Figures 52 and 53 were obtained in this way, and they show the expected decrease in saturation leakage current and production effectiveness at low beam energies. Since neither of these sets of data can be fit based on f(E) alone and since the fits shown are reasonable, the model in which traps are located at the interface appears just as tenable as the one seemingly implied by the saturation data, namely that the traps are distributed.

An additional experiment was performed to examine the reduction process. Leakage current induced by means of a relatively penetrating 30-keV beam was reduced by means of a 12-keV zero-bias irradiation. Full recovery was observed, which confirms that if hole traps are distributed, electron injection is the dominant recovery mechanism. Trap depopulation would not result in complete elimination of distributed trapped charge using the less-penetrating beam.

4.4 DISCUSSION

Results of the present study suggest the following model for radiation-induced production and reduction of back-channel leakage current in n-channel SOS transistors. Ionizing radiation which penetrates into the sapphire substrate generates electron-hole pairs therein. When a drain-to-source bias is applied, a fringing field exists in the sapphire.[44] By analogy with phenomena in irradiated SiO_2 layers,[45] we postulate that this fringing field serves to sweep electrons out of the Al_2O_3 while holes are trapped. For the case of spatially distributed traps, the holes will be trapped very near their point of generation. If all the traps are at the Si-Al_2O_3 interface, then the fringing field will drive a portion of the holes to these sites where they are trapped. The fraction of generated pairs which recombines before electron sweepout occurs should decrease with increasing fringing field (i.e., increasing V_{ds}), and thus the density of trapped holes should also increase. That is, I_ℓ should increase with V_{ds} in agreement with experiment.[46] As the dose deposited in the sapphire increases for a fixed value of V_{ds}, I_ℓ will increase and reach saturation when all hole traps are filled, or, more generally, when a balance is reached between trapping and detrapping events. If irradiation is continued to high doses ($\gtrsim 10^6$ rads(Si)), negatively charged states will form at the Si-Al_2O_3 interface which will serve to reduce I_ℓ below its saturation value.

For a given value of V_{ds}, the fringing field strength decreases with distance into the sapphire. Hence, under the above description, the resulting trapped hole concentration would also decrease with distance into the sapphire under the assumption of a spatial trap distribution. The present results reveal that the first 2 μm of the sapphire is the important region in the I_ℓ production process. However, it is not yet clear whether this depth is determined by a fall-off in pair generation probability, as governed by the fringing field, or by the range of traps in the sapphire. (This could be determined by repeating the present experiments with different drain biases.) After leakage-current saturation is achieved by irradiation to some high dose with V_{ds} applied, continuing the irradiation with $V_{ds} = 0$ causes I_ℓ to reduce to near its pre-irradiation value. If the traps are spatially distributed, then the recovery mechanism is injection of electrons from the silicon into the sapphire where they recombine with trapped holes. Injected electrons drift in the Coulomb field of the trapped charge and thus can neutralize holes trapped some

---

[44] R.A. Kjar and G. Kinoshita, IEEE Trans. Nucl. Sci. <u>20</u>, 315 (Dec. 1973).

[45] J.R. Srour, O.L. Curtis, Jr., and K.Y. Chiu, IEEE Trans. Nucl. Sci. <u>21</u>, 73 (Dec. 1974).

[46] J.L. Peel et al., IEEE Trans. Nucl. Sci. <u>22</u>, 2185 (1975).

distance from the interface. If the traps are located at the interface, then the recovery mechanisms are electron injection and/or radiation-induced trap depopulation.

Harari,[38] Wang and Royce,[47] and Williams et al.[48] have performed optical experiments in which radiation-induced leakage current in n-channel SOS transistors was significantly reduced by illuminating the sapphire substrate under conditions of zero drain bias. Recovery under 3.6 eV illumination was ascribed by Harari to electron injection from Si into Al_2O_3. Wang[47] and Williams[48] observed recovery under 2.5 eV illumination which was attributed to photodepopulation of trapped holes. In principle, it is possible to isolate the depopulation process from the injection process using optical methods. For electron-beam excitation, both recovery mechanisms are energetically allowed under all experimental conditions.

Habing and Shafer[49] observed radiation-induced reduction of built-up positive charge in the gate oxide of CMOS-on-bulk-silicon devices when devices previously irradiated under positive gate bias were further irradiated with zero gate bias. They postulated electron injection from Si into SiO_2 as the recovery mechanism, and their results appear to be analogous to the present observation of back-channel leakage current reduction.

The most attractive phenomenological explanation for differences between the radiation response of wet- and dry-oxide devices was judged here to be the existence of a larger trap density in the dry-oxide case. The only processing difference was the gate oxide growth temperature and time. EerNisse and Derbenwick[50] have developed a model for the radiation sensitivity of the SiO_2-Si system involving interfacial stress. They postulate that production of hole traps in the oxide is related to viscous shear flow. It is not presently clear whether their model could account for significant hole trap density differences in two Si-Al_2O_3 systems

---

[38] E. Harari, Appl. Phys. Letters 29, 25 (1976).

[47] S.T. Wang and B.S.H. Royce, IEEE Trans. Nucl. Sci. 23, 1586 (1976).

[48] R.A. Williams et al., AFCRL-TR-75-0320, May 1975.

[49] D.H. Habing and B.D. Shafer, IEEE Trans. Nucl. Sci. 20, 307 (Dec. 1973).

[50] E.P. EerNisse and G.F. Derbenwick, IEEE Trans. Nucl. Sci. 23, 1534 (1976).

which experienced somewhat different high-temperature treatments (925°C for 60 min versus 1000°C for 150 min). This appears to be a worthwhile point to pursue since if their model were successful in explaining such differences it then might become clear how to optimize SOS processing in terms of minimizing radiation-induced leakage current.

4.5 CONCLUSIONS

Major observations made and conclusions reached in this study are the following: (a) the same functional dependence of radiation-induced leakage current on ionizing dose is exhibited for devices with wet and dry gate oxides; (b) differences in the radiation sensitivity of wet- and dry-oxide devices were attributed to a larger density of hole traps in the sapphire for dry-oxide devices; (c) the temperature dependence of leakage current was attributed to that of back-channel carrier mobility in all cases except for unirradiated wet-oxide devices at room temperature and above where thermal generation dominates; (d) reduction of radiation-induced leakage current to near its pre-irradiation value can be readily accomplished by continuing to irradiate a device with $V_{ds} = 0$; (e) energy must be deposited in the sapphire before radiation-induced increases in leakage current will be observed; (f) energy deposition in the sapphire bulk (i.e., several μm from the interface) is unimportant in terms of giving rise to leakage current; the region which is effective in producing such currents extends into the sapphire a distance on the order of 2 μm from the interface for a drain bias of 5V; (g) if hole traps are spatially distributed, injection of electrons from Si into Al_2O_3 is the dominant recovery mechanism in the process of radiation-induced reduction of leakage current.

SECTION 5.0

MOS HARDENING APPROACHES FOR LOW-TEMPERATURE APPLICATIONS*

5.1 INTRODUCTION

Various low-temperature applications of MOS devices have arisen in the past few years, including amplification, signal processing, and infrared imaging. Charge transfer devices (CTDs) and MOS transistors are used in these applications at operating temperatures less than 100K. If such devices are also employed in an ionizing radiation environment, behavior can differ appreciably from that for room-temperature operation. In particular, theshold voltage shifts in irradiated MOS transistors (or flatband voltage shifts in MOS capacitors) are significantly larger at low temperatures than at room temperature for devices containing SiO_2 gate insulators.[51-56] The reason for this is that holes generated in the oxide by ionizing radiation are relatively immobile at low temperatures except when the electric field applied to the oxide during irradiation is high ($> 2 \times 10^6$ V/cm).[55] At lower fields, those electrons generated during irradiation that escape recombination are swept out of the oxide, leaving behind a trapped hole population which gives rise to large threshold shifts. A hole that does not recombine at low temperatures is trapped very near its point of generation. It is also noteworthy that MOS devices which are

---

*Published in the IEEE Transactions on Nuclear Science 24, 2140 (1977).

[51] R.L. Nielsen and D.K. Nichols, IEEE Trans. Nucl. Sci. 20, 319 (Dec. 1973).

[52] E. Harari, S. Wang, and B.S.H. Royce, J. Appl. Phys. 46, 1310 (1975).

[53] H.H. Sander and B.L. Gregory, IEEE Trans. Nucl. Sci. 22, 2157 (1975).

[54] H.E. Boesch, Jr., F.B. McLean, J.M. McGarrity, and G.A. Ausman, Jr., IEEE Trans. Nucl. Sci. 22, 2163 (1975).

[55] J.R. Srour, S. Othmer, O.L. Curtis, Jr., and K.Y. Chiu, IEEE Trans. Nucl. Sci. 23, 1513 (1976).

[56] H.E. Boesch, Jr., and J.M. McGarrity, IEEE Trans. Nucl. Sci. 23, 1520 (1976).

radiation tolerant at room temperature exhibit significant radiation-induced changes at low temperatures.[55]

This section discusses approaches for reducing the sensitivity of MOS devices to low-temperature charge buildup. Included are analytical and experimental results relating to potential hardening techniques. Results presented herein should be useful in the development of radiation-tolerant MOS devices for low-temperature applications.

5.2 HARDENING APPROACHES

The basic effects of total ionizing dose on an MOS device are charge buildup in the oxide layer and interface state production at the SiO_2-Si interface. Both of these effects give rise to flatband and threshold voltage shifts; additionally, interface state creation causes channel mobility reduction in transistors and increases in dark current and transfer inefficiency in CTDs. As mentioned above, charge buildup in SiO_2 films is significantly more severe at low temperatures than at room temperature. An understanding of the basic mechanisms associated with this phenomenon leads us to suggest the following approaches to alleviating charge buildup problems at low temperatures: (1) carefully select the field applied to the oxide; (2) ion implant the oxide; (3) use a thin oxide; (4) use an insulating film other than SiO_2. This last item is not pursued here. Such an approach may prove to be impractical, but it should be noted that Boesch has observed Al_2O_3 films on silicon to be significantly more radiation tolerant at low temperatures than their SiO_2 counterparts.[57]

The first potential hardening approach -- selection of applied field -- arose from the observation that holes are mobile at high fields in SiO_2 films irradiated at low temperatures.[55] Transporting holes out of the oxide reduces the threshold shift in an irradiated transistor. We have explored this concept through experiment and analysis and findings are presented below. Regarding the approach of hardening by ion implanting the oxide, previous data[55] showed that improved radiation tolerance can be achieved by this method. In the present work, further analysis of ion implantation effects is

---

[55] J.R. Srour, S. Othmer, O.L. Curtis, Jr., and K.Y. Chiu, IEEE Trans. Nucl. Sci. 23, 1513 (1976).

[57] H. E. Boesch, Jr., IEEE Trans. Nucl. Sci. 24, 2135 (1977).

given, including a treatment of the effect of implantation depth on oxide hardness. The third hardening approach -- use of a thin oxide -- is beneficial for devices operated at room temperature.[58] This same procedure is also applicable for low-temperature operation because the total amount of positive charge trapped throughout the oxide decreases with decreasing thickness and therefore threshold voltage shift will also decrease.[53] We treat these three topics in turn.

5.3 EFFECTS OF APPLIED FIELD

5.3.1 Experimental Results

Experiments were performed to examine the applied field dependence of low-temperature charge buildup in SiO_2 films. Test vehicles for this study were MOS capacitors fabricated by Hughes Aircraft using procedures developed by Aubuchon.[59] These Al-gate devices contained a dry thermal oxide (910 Å) on an n-type silicon substrate (2 to 5 Ω-cm). Irradiations were performed at both room temperature and 77 K using the Co^{60} source at Northrop Research and Technology Center. The dose rate for these experiments was 40 rads(Si)/s as determined by CaF_2 thermoluminescent dosimeters. Flatband voltage was determined at several total doses for each device from <u>in situ</u> capacitance-vs-voltage measurements made with a PAR Model 410 CV plotter (1 MHz).

Figure 55 shows flatband voltage shift at 10^5 rads(Si) versus voltage applied during irradiation for a group of identical MOS capacitors. Data are shown for 77 K and room temperature and each data point was obtained from measurements on a single device. That is, forty devices were used to acquire the data. Figure 56 shows similar data after a total dose of 10^6 rads(Si) for the same devices represented in Figure 55. For +10V applied, the 77 K voltage shift at this dose is a factor of 7.5 larger than that at room temperature. For an applied voltage somewhat less than or considerably greater than +10V, the flatband shift at 77 K is significantly less than the peak value.

---

[53] H.H. Sander and B.L. Gregory, IEEE Trans. Nucl. Sci. <u>22</u>, 2157 (1975).

[58] G.F. Derbenwick and B.L. Gregory, IEEE Trans. Nucl. Sci. <u>22</u>, 2151 (1975).

[59] K.G. Aubuchon, IEEE Trans. Nucl. Sci. <u>18</u>, 117 (Dec. 1971).

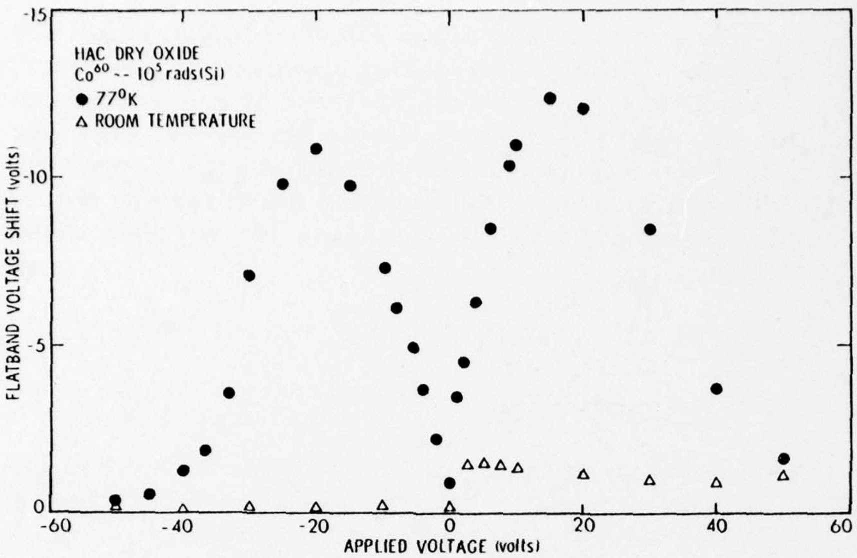

Figure 55. Flatband voltage shift at 10^5 rads(Si) vs applied voltage for MOS capacitors irradiated at 77 K and at room temperature at a dose rate of 40 rads(Si)/s.

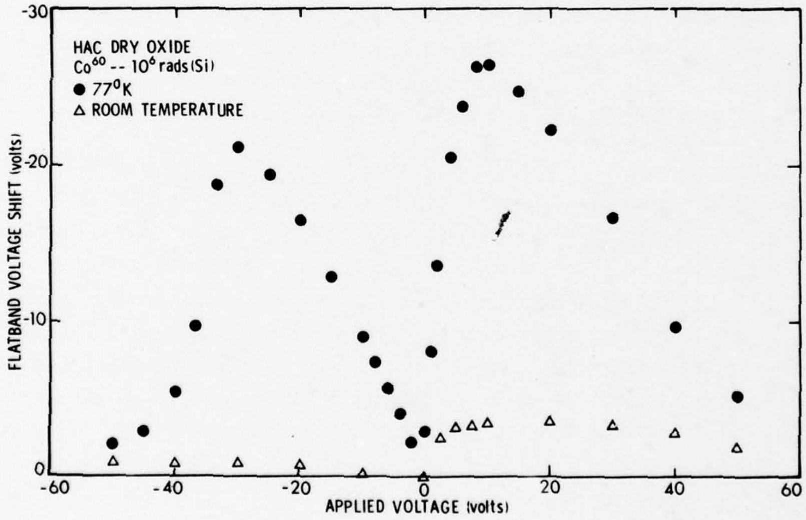

Figure 56. Flatband voltage shift at 10^6 rads(Si) vs applied voltage for MOS capacitors irradiated at 77 K and at room temperature at a dose rate of 40 rads(Si)/s.

Negative bias results for the present devices (n-type substrate) should be indicative of behavior expected for an enhancement-mode p-channel transistor. For this application, it is seen that the oxide film studied is indeed radiation resistant at room temperature. At an applied voltage of -10V, after 10^6 rads, the flatband voltage shift is quite small (~0.3V). On the other hand, under the same conditions the flatband shift at 77 K is 9V, a factor of thirty larger than at room temperature. The present data again demonstrate that SiO_2 films which are resistant to ionizing radiation effects at room temperature will experience significant charge buildup at low temperatures.

The rather interesting double-hump structure of low-temperature data in Figures 55 and 56 can be understood qualitatively as follows. At low fields ($< 2 \times 10^6$ V/cm) a portion of the electron-hole pairs generated by radiation in the oxide film recombine. Electrons escaping recombination are swept out while remaining holes are "frozen in." As the field is increased, a larger fraction of electrons escapes recombination leaving an increasingly larger amount of uniformly-distributed positive charge. Thus, the flatband shift ΔV_{fb} at a given dose increases with increasing applied voltage. At higher fields, the holes become mobile which results in less positive charge in the oxide and thus gives rise to the observed decrease in ΔV_{fb} with increasing bias.

It is important to note that the high-field data of Figures 55 and 56 are only applicable to the case of a relatively low steady-state ionizing dose rate and do not apply at early times following pulsed bombardment. This point is made clear in Figure 57 where the fraction of generated holes collected at time t after an ionizing burst (10-μs pulse of 5-keV electrons) is plotted versus temperature for several values of t. (Information in Figure 57 is based on data in Ref. 55.) The data shown are for a relatively high value of applied field (4×10^6 V/cm). At 90 K, very few holes have been transported to the electrodes at early times following the burst and thus ΔV_{fb} will be large for high doses. At $t = 10$ sec, a significant amount of hole transport has taken place so ΔV_{fb} will be significantly less than at early times. The data of Figure 55 were obtained after a 42-min irradiation and therefore considerable hole transport occurred at high fields during bombardment.

---

[55] J.R. Srour, S. Othmer, O.L. Curtis, Jr., and K.Y. Chiu, IEEE Trans. Nucl. Sci. 23, 1513 (1976).

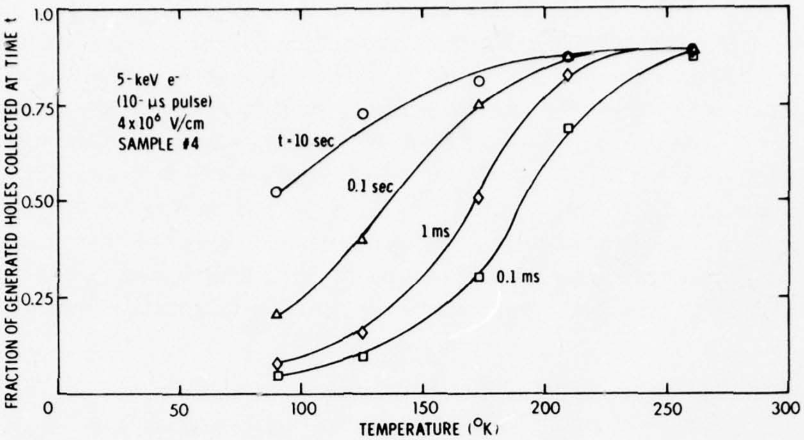

Figure 57. Fraction of generated holes collected in an MOS capacitor at time t following a pulse of ionizing radiation at various temperatures. (Information shown here is based on data in Ref. 55.)

5.3.2 Analysis of Applied Field Effects

A quantitative framework for describing the data in Figures 55 and 56 is now presented. As a starting point, we assume for an MOS capacitor (unimplanted) in an ionizing radiation environment that all electrons generated in the oxide which escape initial recombination* are swept out, leaving behind trapped holes. Consider an oxide layer of thickness t_{ox} in such a device. If a uniform trapped hole concentration ρ exists throughout the oxide, the resulting flatband shift is given by

---

*Initial recombination is usually taken to be synonymous with geminate recombination. In a given situation, columnar (or "track") recombination may also be important (see Refs. 60 and 45). We use the term "initial" loosely here to denote the dominant recombination mechanism at early times following pair generation.

[45] J.R. Srour, O.L. Curtis, Jr., and K.Y. Chiu, IEEE Trans. Nucl. Sci. <u>21</u>, 73 (Dec. 1974).

[55] J.R. Srour, S. Othmer, O.L. Curtis, Jr., and K.Y. Chiu, IEEE Trans. Nucl. Sci. <u>23</u>, 1513 (1976).

[60] R.C. Hughes, IEEE Trans. Nucl. Sci. <u>18</u>, 281 (Dec. 1971).

$$\Delta V_{fb} = \left(\frac{\rho}{2\epsilon}\right) t_{ox}^2 . \qquad (1)$$

If initial recombination of holes is neglected, the total positive charge density generated by ionizing radiation can be calculated by assuming 18 eV/pair (translates to 7.9×10^{12} pairs/cm^{3}rad for SiO_2). Then, in terms of ionizing dose γ in rads(Si), the quantity ρ in coul/cm^3 can be expressed as $1.26 \times 10^{-6}\ \gamma$. Flat-band voltage shift in Eq. (1) is then given by $1.82 \times 10^6\ \gamma t_{ox}^2$ volts, where t_{ox} is in cm.

Hole motion is now taken into account. The following simple model was considered first. At $t = 0$, electron-hole pairs are generated uniformly in the oxide. At $t = 0^+$, a portion of those pairs have already recombined and all of the remaining electrons are swept out, leaving a uniform "frozen-in" hole distribution. For high applied fields ($> 2 \times 10^6$ V/cm), hole transport occurs.[55] At such fields, initial recombination is negligible (discussed below) and thus all generated holes remain in the oxide at $t = 0^+$. In this simple model, the entire distribution of holes is assumed to move uniformly through the oxide. For example, under positive bias the hole population moves a "transport distance" d_t toward the SiO_2-Si interface in a time t_1.

The model described above was pursued and found to be unsatisfactory in accounting for the data of Figures 55 and 56. Specifically, in determining those values of transport distance d_t required to fit ΔV_{fb} data, it was found that both the magnitude of d_t at a given field and its functional dependence on applied field disagreed significantly when results for positive and negative bias were compared. This physically unrealistic result led us to employ a more meaningful model in which a distribution of hole mobilities is taken into account. That is, at a given time following carrier excitation the more mobiles holes have been swept out of the oxide while their less mobile counterparts remain there until some later time. Such a viewpoint is consistent with both the multiple-trapping model[55, 61] and the CTRW model[23, 54] of charge transport in SiO_2.

---

[23] F.B. McLean, H.E. Boesch, Jr., and J.M. McGarrity, IEEE Trans. Nucl. Sci. 23, 1506 (1976).

[54] H.E. Boesch, Jr., F.B. McLean, J.M. McGarrity, and G.A. Ausman, Jr., IEEE Trans. Nucl. Sci. 22, 2163 (1975).

[55] J.R. Srour, S. Othmer, O.L. Curtis, Jr., and K.Y. Chiu, IEEE Trans. Nucl. Sci. 23, 1513 (1976).

[61] O.L. Curtis, Jr., and J.R. Srour, J. Appl. Phys. 48, 3819 (1977).

Figure 58 illustrates this more realistic transport model. Shown is an MOS capacitor with a charge density ρ, dependent on distance x, superimposed on the oxide. The solid line depicts the charge distribution at a particular time after excitation and we characterize this distribution in terms of a transport distance d_t as in the simple model. However, d_t is now defined differently as shown in the figure. Additionally, it is assumed that when $d_t = t_{ox}/2$, then ρ is equal to its maximum value ρ_0 only at the SiO_2-Si interface. That is, the "slope" of the charge distribution is assumed to remain constant as charge is swept out of the oxide. The solid line in Figure 58 corresponds to a value for d_t less than $t_{ox}/2$. Also shown for illustration (dashed) are two other cases: $d_t = t_{ox}/2$ and $d_t > t_{ox}/2$.

Expressions for flatband voltage shift in terms of transport distance for the model depicted in Figure 58 are now given. Under an applied positive bias, for $d_t \leq t_{ox}/2$:

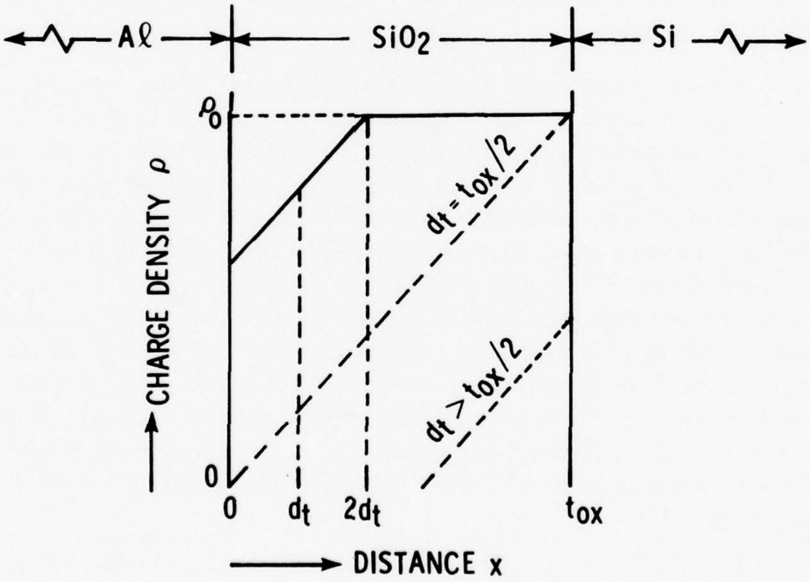

Figure 58. Illustration of a more realistic model for hole motion at high fields and low temperatures in SiO_2 (positive bias case). Shown are three hole distributions corresponding to three values of transport distance d_t.

$$\Delta V_{fb} = \frac{\rho_0}{\varepsilon t_{ox}} \left(\frac{1}{2} t_{ox}^3 - \frac{4}{3} d_t^3 \right) . \qquad (2)$$

For $d_t \geq t_{ox}/2$:

$$\Delta V_{fb} = \frac{\rho_0}{\varepsilon t_{ox}} \left(\frac{2}{3} t_{ox}^3 - 2 t_{ox} d_t^2 + \frac{4}{3} d_t^3 \right) . \qquad (3)$$

For the case of an applied negative bias, the hole distributions are of the same form as those in Figure 58 except that now we define d_t in terms of distance from the SiO_2-Si interface. For $d_t \leq t_{ox}/2$, we obtain

$$\Delta V_{fb} = \frac{\rho_0}{\varepsilon t_{ox}} \left(\frac{4}{3} d_t^3 - 2 d_t^2 t_{ox} + \frac{1}{2} t_{ox}^3 \right), \qquad (4)$$

and for $d_t \geq t_{ox}/2$

$$\Delta V_{fb} = \frac{4}{3} \frac{\rho_0}{\varepsilon t_{ox}} \left(t_{ox} - d_t \right)^3 . \qquad (5)$$

Equations (2) through (5) can be viewed as yielding the temporal dependence of ΔV_{fb} since d_t is a function of time following bombardment. For a fixed time following bombardment, variations in d_t can be obtained by applying different values of field to a set of samples irradiated and measured under otherwise identical conditions.

As mentioned previously,[55] a complication arises when comparing expected and measured flatband voltage shifts at low temperatures for doses greater than $\sim 10^5$ rads(Si). At such doses, the oxide field will be perturbed due to the substantial charge buildup that exists. This perturbation is manifested as a decrease in field near the metal-SiO_2 interface and an increase in field near the SiO_2-Si interface. In the increased field region, hole transport will occur if the field there is greater than 2×10^6 V/cm. In the decreased field region, more initial recombination of generated electron-hole pairs will occur. Flatband voltage shifts will be reduced by both of these mechanisms relative to values expected on the basis of a uniform field throughout the oxide. Hence, in analysis of the present

---

[55] J.R. Srour, S. Othmer, O.L. Curtis, Jr., and K.Y. Chiu, IEEE Trans. Nucl. Sci. 23, 1513 (1976).

experimental results we only treat data obtained at 10^5 rads(Si) (Figure 55) in an attempt to avoid these complications. (Calculations by Boesch and McGarrity[56] for an oxide of thickness similar to that utilized here indicate non-negligible field modification at 10^5 rads(Si) for a device irradiated at 80 K with a 10V bias. Assuming that their calculations apply quantitatively to the present experimental conditions, it still appears likely that the predicted field perturbation for this dose would not significantly alter conclusions made below which are based on data fitting with the model of Figure 58.)

Analysis of low-temperature flatband shift versus applied voltage data in Figure 55 was performed using Eqs. (1) through (5). At 10^5 rads(Si) for an oxide thickness of 910 Å, Eq. (1) yields ΔV_{fb} = 15.2V. That is, the maximum predicted value of ΔV_{fb} is 15.2V and this value should result when all holes generated in the oxide at 10^5 rads are trapped without being transported and all generated electrons are swept out. Measured ΔV_{fb} arises from holes trapped in the oxide and the amount and distribution of these trapped charges can be attributed to two field-dependent effects. First, the number of holes available for contributing to ΔV_{fb} depends on the amount of initial recombination that has occurred. That is, the dependence of electron yield on applied field is important. As yield increases, ΔV_{fb} increases. Second, at high fields holes are transported out of the oxide, thereby reducing ΔV_{fb}.

Boesch and McGarrity[56] determined the field dependence of electron yield* for MOS capacitors irradiated at 80 K by measuring ΔV_{fb} at early times following pulsed excitation (4-μs pulse of 13-MeV electrons). For fields $> 2 \times 10^6$ V/cm, they observed a nearly saturated yield corresponding to sweepout of nearly all the electrons generated. At such fields, apparently all generated electrons escape initial recombination and are swept out of the oxide. For

---

*For MOS capacitors irradiated at low temperatures, we prefer to ascribe the increase in ΔV_{fb} with field to an increase in "electron yield" since the number of electrons escaping recombination and being swept out of the oxide increases with field. One could also describe the same situation in terms of "hole yield" since the number of trapped holes also increases with field (except at high fields) and gives rise to increases in ΔV_{fb}. Boesch[56] used the latter nomenclature.

[56] H. E. Boesch, Jr., and J.M. McGarrity, IEEE Trans. Nucl. Sci. 23, 1520 (1976).

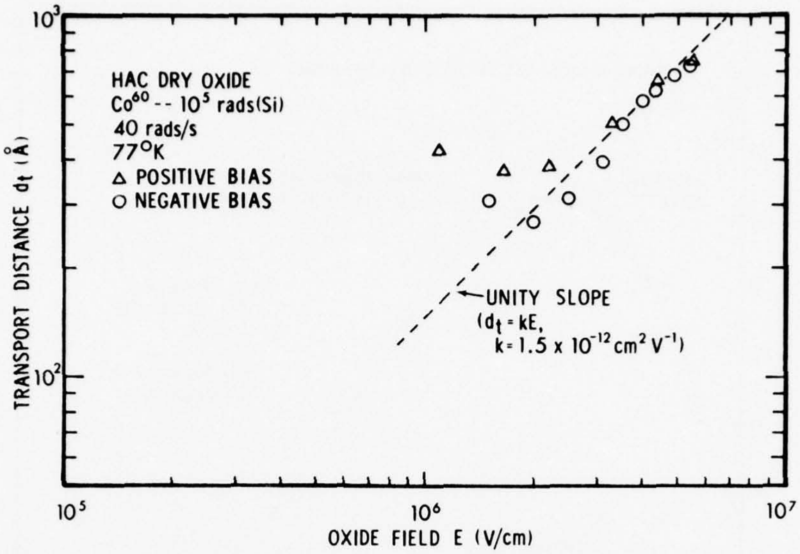

Figure 59. Transport distance vs applied field based on calculations using the model illustrated in Figure 58.

this regime, ΔV_{fb} can be attributed to the entire generated hole population modified by transport according to the model of Figure 58.

An iterative procedure was used in conjunction with Eqs. (2) and (5) to calculate transport distance d_t based on measured values of ΔV_{fb} at 10^5 rads (77 K data of Figure 55). Figure 59 shows results of these calculations in terms of d_t versus oxide field. For fields $> 3 \times 10^6$ V/cm, positive and negative bias results are in good agreement. As mentioned above, such agreement is expected for a physically meaningful model. These high-field results are fit reasonably well with a unity-slope line. At lower fields, deviation of the calculated points from this line is due to the influence of electron yield. That is, Eqs. (2) through (5) assume that all generated electrons have been swept out which is not the case at lower fields. The unity-slope fit yields $d_t = kE$, where $k = 1.5 \times 10^{-12}$ cm^2V^{-1}. This expression was then used to fit positive bias flatband shift data. Equations (2) and (3) were utilized to obtain an appropriate charge transport curve and the result is shown in Figure 60. The next step was to empirically fit a yield-vs-field curve to the low-field data. The criterion employed was to obtain a curve that, when considered simultaneously with the charge transport curve, would yield a good composite fit to the experimental data. The resulting curve is shown in Figure 60 along with the composite fit (solid curve). (To obtain

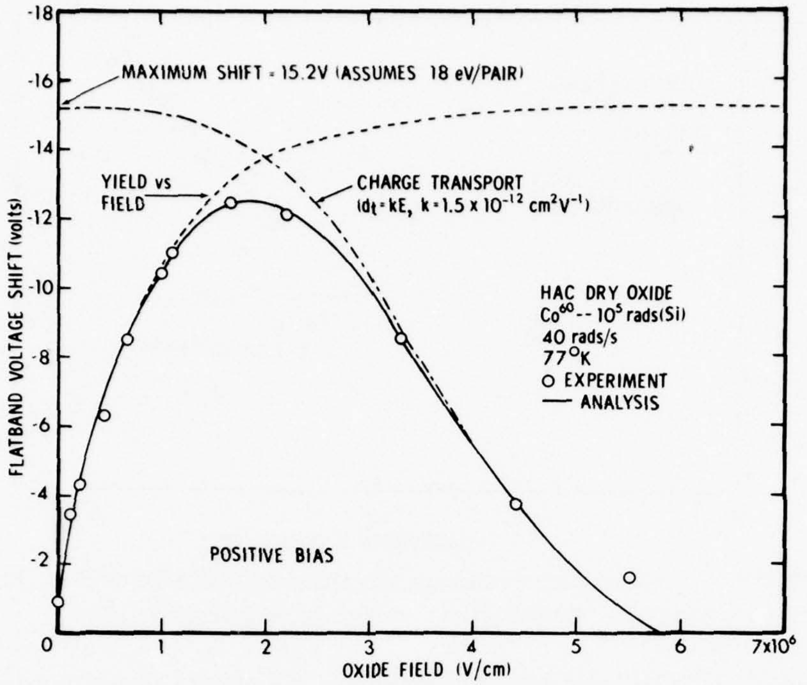

Figure 60. Flatband voltage shift at 77 K vs oxide field for the case of an applied positive bias. Results of data fitting using the charge transport model of Figure 58 in conjunction with a yield-vs-field component are shown.

this fit, the charge transport curve is multiplied by the yield-vs-field curve normalized to its saturation value.) By considering the charge-transport and the yield-vs-field mechanisms jointly, an excellent fit to the applied field dependence of flatband voltage shift at 77 K is obtained.

The same fitting procedure was also applied to negative bias data. A charge transport curve fit the highest-field data but deviated from the data at intermediate fields. Reducing k to 1.4 x 10^{12} improved the transport fit somewhat. A rather severe linear yield-vs-field curve was required, in conjunction with either of these transport curves, to obtain a fit for data at fields $< 2 \times 10^6$ V/cm. A composite fit exhibited a good fit to the data for fields $\leq 10^6$ V/cm and $> 3 \times 10^6$ V/cm. The peak of the composite fit occurred at a somewhat lower field than exhibited by the data. Although the general features of the negative bias data are well described by the modeling approach employed, the fit obtained was not as good as that for positive bias.

The influence of an initial transport distance d_o on the data fitting procedure was considered. Boesch and McGarrity[56] observed that initial flatband shifts at 80 K differed slightly depending on the polarity of the applied bias. They account for this observation in terms of an initial transport of holes in the valence band subsequent to thermalization but before the first capture event. It seems reasonable to expect that d_o will vary directly with applied field and thus correspond to an initial Schubweg. Treated in this manner, d_o was found to have negligible effect on the fitting procedures used here for positive bias data. For negative bias, an initial Schubweg has an important effect. However, such a modification to the fitting procedure actually caused the fit at high fields to be worse than without this correction.

It is of interest to compare the yield-vs-field curve in Figure 60 with previous findings. Figure 61 shows this curve along with that obtained by Boesch.[56] The shape of the two curves is nearly the same and excellent agreement is noted for fields $\geqslant 2 \times 10^6$ V/cm. This agreement supports the validity of the present modeling approach. Boesch obtained the solid curve of Figure 61 by measuring ΔV_{fb} shortly (~1 ms) after a pulse of ionizing radiation. At such times, the dependence of ΔV_{fb} on applied field follows the electron yield-vs-field curve because hole transport is negligible. At much later times, or in a steady-state ionizing radiation environment, data such as that in Figures 55 and 56 are obtained.

It is perhaps surprising that transport distance was observed to depend linearly on field for data of both polarities in Figure 59. Such a dependence yields an effective hole mobility that is <u>independent</u> of field. To obtain a rough estimate of mobility, a characteristic time of 21 min. (i.e., one-half the time it takes to deliver 10^5 rads at a rate of 40 rads/s) was assumed. From Figure 59, $d(d_t)/dE = k_1 = 1.5 \times 10^{-12}$ cm^{2}V^{-1}, which yields an estimated mobility of ~10^{-15} cm^2/Vsec. This observation is in contrast to previous results[55,61] in which mobility was noted to depend on E^3 at intermediate temperatures and on E^{13} at low temperature (90 K). However,

---

[55] J.R. Srour, S. Othmer, O.L. Curtis, Jr., and K.Y. Chiu, IEEE Trans. Nucl. Sci. 23, 1513 (1976).

[56] H.E. Boesch, Jr., and J.M. McGarrity, IEEE Trans. Nucl. Sci. 23, 1520 (1976).

[61] O.L. Curtis, Jr., and J.R.Srour, J. Appl. Phys. 48, 3819 (1977).

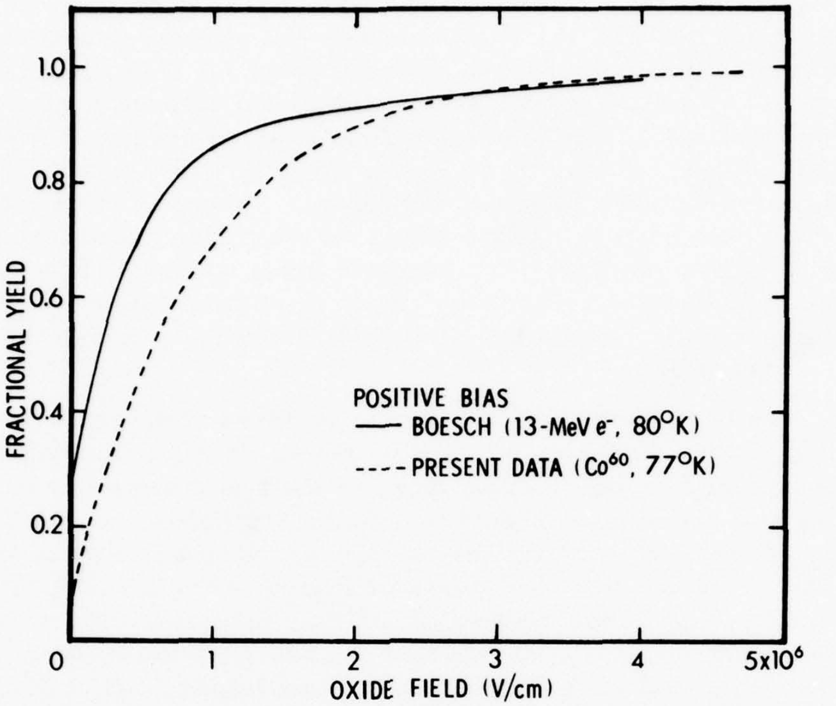

Figure 61. Fractional yield vs oxide field for the present study (from Figure 60) and for that of Boesch and McGarrity.[56]

mobility was derived in a different manner than in the cited work. In the present case, a quantity related to carrier transport was measured at a <u>fixed time</u> following bombardment whereas in previous determinations a <u>fixed amount of transported charge</u> was used as the basis for evaluating mobility. We have found that evaluating field-dependent transport data by these two methods can yield significantly different results and this feature may be responsible for observations of a field-independent mobility in one case and a strong field dependence in other cases. The fact that test specimens used in the present study were different from those employed in previous work may also be important. The most important observation to be made, however, is that the region of apparent linearity in Figure 59 is fairly narrow. At low fields the dependence of carrier yield on applied field is imporant and at high fields saturation of d_t is expected. These two effects possibly mask a nonlinear dependence of transport distance on field and, thus, a field-dependent mobility.

---

[56] H.E. Boesch, Jr., and J.M. McGarrity, IEEE Trans. Nucl. Sci. 23, 1520 (1976).

5.4 EFFECTS OF ION IMPLANTATION

A reasonable approach to reducing the effects of positive charge buildup in SiO_2 films irradiated at low temperatures is to introduce electron traps for compensation. Electron (and hole) traps can be introduced into SiO_2 by ion implantation[62] and we have previously examined charge buildup at 77 K in an Al^+-implanted specimen.[55] A factor of two improvement was observed compared to an unimplanted device. The implantation employed was not optimum since traps were only introduced into that half of the oxide nearer the Al-SiO_2 interface. Analysis of ion implantation effects is presented here which is useful for defining optimum structures and for predicting low-temperature radiation response. (This analysis is an extension of previous work[62] to low-temperature conditions.)

Consider an MOS capacitor with an ion-implanted oxide. We denote the implantation depth as d_i (measured from the metal-SiO_2 interface) and the region between this interface and d_i is assumed to be uniformly damaged, i.e., to contain a uniform trap concentration. The mean electron range (Schubweg) ω_e in the implanted zone between the metal-SiO_2 interface and d_i is given by $\mu_e \tau_e E$, where μ_e and τ_e are mobility and lifetime, respectively, and E is applied electric field. It is assumed that at low temperatures all holes generated in the oxide by ionizing radiation in both the implanted and unimplanted zones are immobile. All electrons generated in the unimplanted zone are assumed to be completely swept out of that region, either into the implanted zone or into the silicon depending on the polarity of the applied bias. The case of a positive bias applied to the metal electrode is considered here.

Electrons generated in the implanted region will move an average distance ω_e toward the metal electrode before being permanently trapped. Thus, the average position of these trapped electrons is a distance $(d_i - \omega_e)/2$ from the metal-SiO_2 interface. Electrons generated in the unimplanted region of the oxide will be swept toward the implanted zone and move an average distance ω_e into this region before being permanently trapped. The average position of these trapped electrons is a distance $d_i - \omega_e$ from the

---

[55] J.R. Srour, S. Othmer, O.L. Curtis, Jr., and K.Y. Chiu, IEEE Trans. Nucl. Sci. 23, 1513 (1976).

[62] O.L. Curtis, Jr., J.R. Srour, and K.Y. Chiu, IEEE Trans. Nucl. Sci. 22, 2174 (1975).

metal-SiO_2 interface. Thus, electrons trapped at two average positions in the implanted region will compensate for a portion of the positive charge which, by assumption, is trapped uniformly throughout the oxide.

It is of interest to compare expected flatband voltage shifts for implanted and unimplanted MOS capacitors. For an unimplanted unit, the average position of the trapped positive charge is at $t_{ox}/2$. For an implanted sample, the two contributions to ΔV_{fb} from trapped electrons are subtracted from the trapped hole contribution. In addition, different fractions of the total amount of negative charge generated are trapped at the two average positions. It can be shown that the ratio of flatband voltage shifts for implanted and unimplanted specimens is given by

$$\frac{\Delta V_{fb}\,(\text{implanted})}{\Delta V_{fb}\,(\text{unimplanted})} = 1 - \left(\frac{d_i - \omega_e}{t_{ox}}\right)\left[2 - \left(\frac{d_i + \omega_e}{t_{ox}}\right)\right]. \qquad (6)$$

Equation (6) relates the expected reduction in ΔV_{fb} accomplished by implantation to both the Schubweg in the implanted zone and the implantation depth. In order to perform example calculations, a value for ω_e is needed. Previous work[62] yielded a $\mu_e \tau_e$ value at room temperature of $\sim 2 \times 10^{-12}$ cm^2V^{-1} for the implanted zone of 20-keV Al^+-implanted specimens (fluence = 10^{15} cm^{-2}). For an applied field of 10^6 V/cm, this value translates to a value for ω_e of 200 Å. We assume that ω_e is temperature independent and thus that the $\mu_e \tau_e$ value obtained at room temperature can be applied at low temperatures. The primary temperature dependence expected is that of capture cross-section and this consideration is neglected here for simplicity. Figure 62 presents results of calculations performed using Eq. (6). The quantity ΔV_{fb}(implanted/ΔV_{fb}(unimplanted) is plotted versus implantation depth for three values of ω_e and an oxide thickness of 1000 Å. The ω_e value of 200 Å was chosen to be representative of conditions for a field of 10^6 V/cm and an implantation fluence of 10^{15} cm^{-2}. The lower values of ω_e were selected to examine the expected effects of higher fluences (i.e., shorter electron Schubweg). The intuitively obvious results were obtained: increasing the ratio of implantation depth to oxide thickness and/or reducing the electron Schubweg

---

[62] O.L. Curtis, Jr., J.R. Srour, and K.Y. Chiu, IEEE Trans. Nucl. Sci. 22, 2174 (1975).

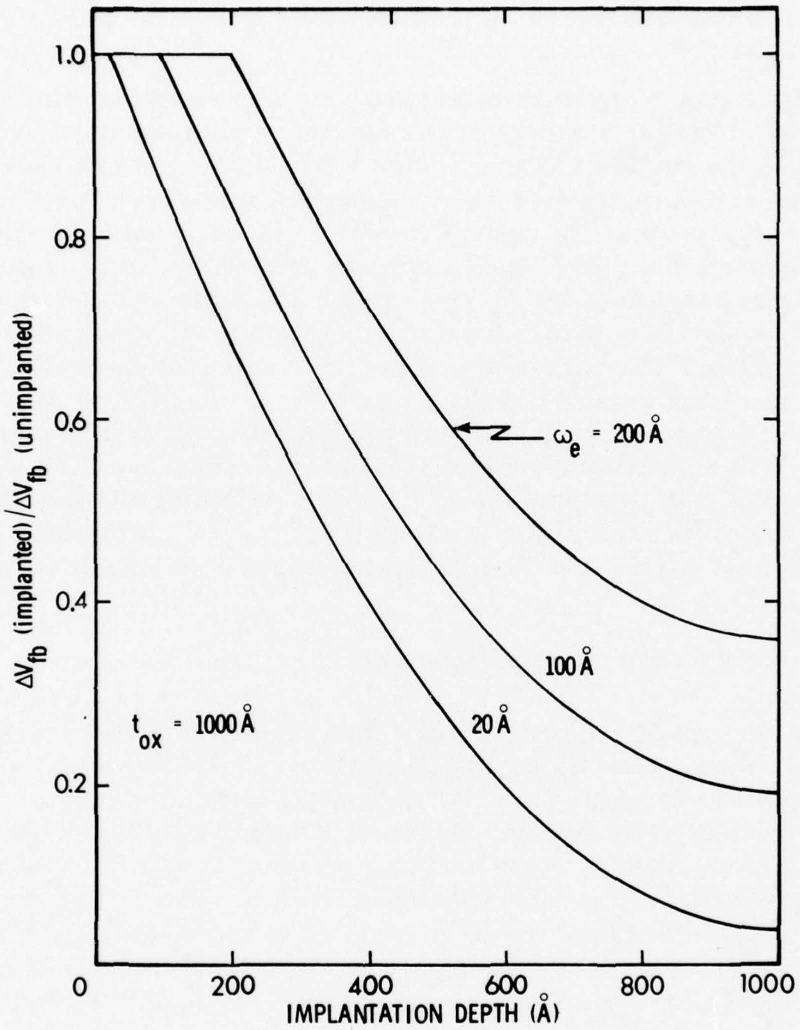

Figure 62. The calculated ratio of ΔV_{fb}(implanted) to ΔV_{fb}(unimplanted) vs implantation depth for three values of electron Schubweg.

reduces ΔV_{fb} for an implanted specimen relative to that for an unimplanted unit. For example, implanting ions to a depth of 800 Å at such a fluence to cause w_e to equal 20 Å is predicted to reduce ΔV_{fb} by a factor of 13.

As the applied field is increased, w_e will increase with the result that a larger fraction of the electrons generated escape being trapped in the implanted zone. This effect will diminish the degree of compensation of trapped positive charge. However, as discussed above, holes are mobile at high fields in unimplanted SiO_2 films at low temperatures. In a more complete analysis of charge compensation and charge buildup in implanted specimens at low temperatures, one should consider motion of holes out of the unimplanted zone into either the silicon substrate or into the implanted region, depending on the polarity of the applied bias. In addition to neglecting hole transport, initial recombination of generated electrons and holes was not considered in the above discussion. The assumption was made in previous work[62] that ion implantation has no effect on the processes of generation and initial recombination of electron-hole pairs, and that same assumption was made here in developing Eq. (6).

5.5 EFFECTS OF OXIDE THICKNESS

The degree of radiation tolerance achievable at low temperatures by reducing the oxide thickness is now considered. Decreasing t_{ox} increases the oxide field for a constant applied voltage. Thus, ΔV_{fb} is reduced in two ways: (1) the total number of holes generated in the oxide decreases; (2) charge transport increases. Sander and Gregory[53] observed threshold voltage shift to vary as t_{ox}^2 for a set of MOS transistors irradiated at 76 K. The model they used to account for this observation is that which leads to Eq. (1). The present work reveals that for high applied fields this simple model is inadequate since significant transport of holes out of the oxide occurs. Equation (1) gives the maximum flatband shift (ΔV_{fb}^m) that can occur at a given dose for a fixed oxide thickness and this maximum results when all electrons generated are swept out and no recombination occurs. Equations (2) through (5) can also be rewritten in terms of ΔV_{fb}^m. Additionally, transport distance d_t is

---

[53] H.H. Sander and B.L. Gregory, IEEE Trans. Nucl. Sci. 22, 2157 (1975).

[62] O.L. Curtis, Jr., J.R. Srour, and K.Y. Chiu, IEEE Trans. Nucl. Sci. 22, 2174 (1975).

given by kE (Figure 59). Also, $E = V/t_{ox}$, where V is applied voltage. Thus, $d_t = kV/t_{ox}$ and Eqs. (2) and (3) can be rewritten as

$$\Delta V_{fb} = \Delta V_{fb}^{m} \left(1 - \frac{8}{3} \frac{(kV)^3}{t_{ox}^6} \right) \qquad (7)$$

for $d_t \leq t_{ox}/2$ (or $t_{ox} \geq (2kV)^{1/2}$), and

$$\Delta V_{fb} = \Delta V_{fb}^{m} \left(\frac{4}{3} - 4 \frac{(kV)^2}{t_{ox}^4} + \frac{8}{3} \frac{(kV)^3}{t_{ox}^6} \right) \qquad (8)$$

for $d_t \geq t_{ox}/2$ (or $t_{ox} \leq (2kV)^{1/2}$). These expressions contain both the thickness and applied-field dependences of low-temperature flatband shift.

When applying Eqs. (7) and (8), it should be noted that all holes have been transported out of the oxide when $d_t = t_{ox}$. This condition can also be expressed as $t_{ox} = (kV)^{1/2}$, thereby giving a minimum value of t_{ox} for which (7) and (8) apply. Figure 63 shows results of calculations using these equations and Eq. (1). The solid curve corresponds to the maximum shift attainable for oxide thicknesses from 300 to 900 Å after 10^5 rads(Si). The dashed curves correspond to various values of applied voltage and these curves reveal the reduction in ΔV_{fb} that occurs due to hole transport.

An example will illustrate the effectiveness of reducing t_{ox} in increasing radiation tolerance. Consider calculations for 900 Å and 450 Å oxides in Figure 63. The maximum shifts are 14.7 and 3.7V for these cases, respectively, and this reduction is due to the t_{ox}^2 dependence of ΔV_{fb}. The reduction in charge buildup is much more dranatic when a field is applied. For 10V applied, the predicted reduction in ΔV_{fb} due to hole transport is insigniicant (14.7V reduces to 14.5V) at 900 Å. However, at 450 Å, the maximum shift of 3.7V is predicted to be reduced to 0.82V. Thus, the present calculations indicate that for an applied voltage of 10V, reducing t_{ox} from 900 to 450 Å will decrease ΔV_{fb} by a factor of ~18. If reliable thin ($\lesssim$500 Å) oxides can be fabricated for use at applied voltages $\gtrsim$10V, then it appears that low-temperature charge buildup problems will be largely eliminated in a steady-state

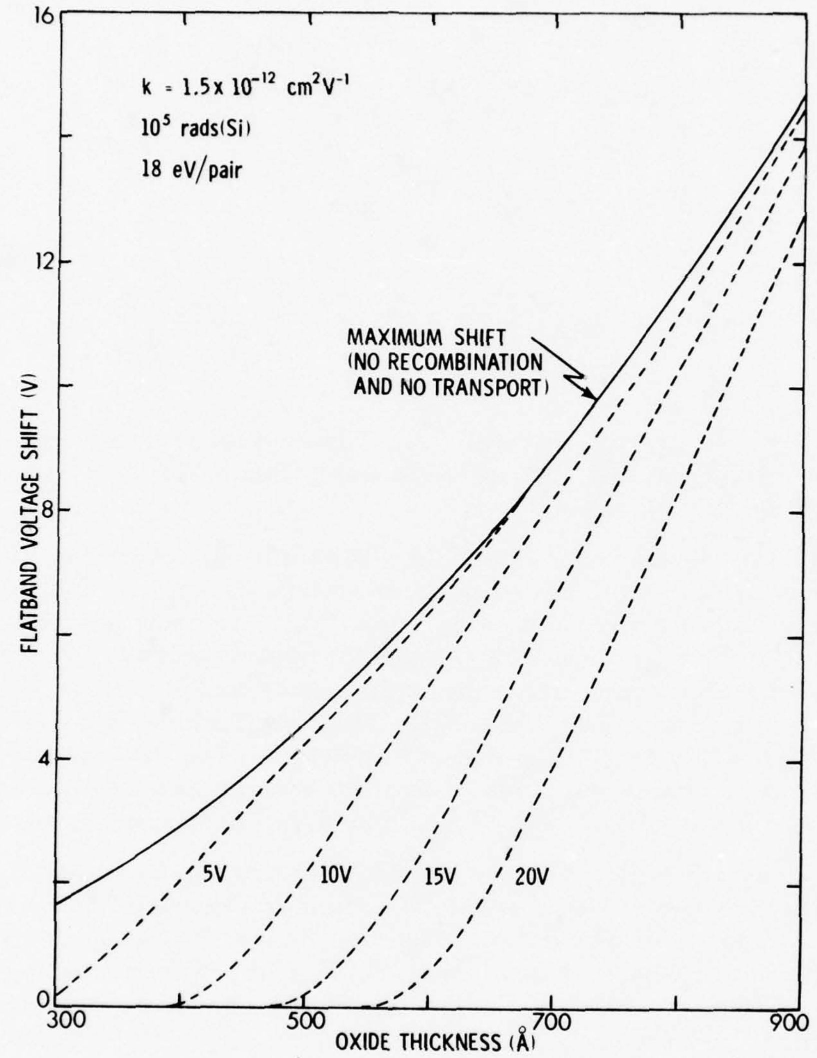

Figure 63. Calculated flatband voltage shift at 10^5 rads(Si) vs oxide thickness for four values of applied voltage. Also shown (solid curve) is the maximum flatband shift which results when there is no recombination and no hole transport.

ionizing radiation environment. However, this hardening approach will not be nearly as effective at early times following pulsed bombardment. For that case, the reduction in ΔV_{fb} that results when t_{ox} is reduced will follow the solid curve of Figure 63.

5.6 SUMMARY AND CONCLUSIONS

We have found that the applied field dependence of flatband voltage shift in MOS capacitors irradiated at 77 K can be accounted for in terms of the field dependence of electron yield and the transport of holes at high fields. Analysis of ion implantation effects indicates that a significant improvement in radiation tolerance should be achievable at low temperatures by this method. A simultaneous consideration of the effects of oxide thickness and applied field on charge buildup in an unimplanted oxide suggests that reducing t_{ox} to ≤ 500 Å will largely eliminate low-temperature problems in a steady-state ionizing radiation environment as long as the applied voltage is ≥ 10V. If such conditions prove to be impractical, then ion implantation may be a valuable hardening procedure. Use of a thin oxide with a relatively high applied field appears to be a more attractive approach to realizing hardened MOS devices for low-temperature applications in a steady-state environment. At early times following pulsed bombardment, this approach will not be as effective.

SECTION 6.0

DETERMINATION OF THE DIFFUSION LENGTH AND DRIFT MOBILITY IN SILICON BY USE OF A MODULATED SEM BEAM*

6.1 INTRODUCTION

The parameters of minority-carrier diffusion length and drift mobility are of importance in all semiconductor devices relying on minority-carrier conduction, such as bipolar transistors and solar cells. When minority carriers are locally injected into a semiconductor, the spatial distribution is governed by the diffusion length and the temporal decay by the lifetime. These quantitities are related by the drift mobility. The lifetime in silicon is found to be extremely sensitive to material imperfections and the concentration of certain impurities. For example, these factors may limit the efficiency of solar cells in that the effective collection volume for generated carriers is given by the diffusion length. Currently, efforts are underway to develop technologies for low-cost silicon solar cells for terrestrial applications. The large cost reduction required compels the use of silicon which is considerably less ideal than that employed in space cells. The material may be marginal in diffusion length, nonhomogeneous or even polycrystalline. In such material, the drift mobility may differ from that expected in high-grade silicon and therefore needs to be characterized in addition to lifetime or diffusion length. If lifetime is measured, moreover, the drift mobility is required to determine the equivalent diffusion length. Since drift mobilities are difficult to obtain experimentally, particularly in materials of short diffusion length, Hall measurements of mobility are generally relied upon. The measured quantity here is the majority-carrier mobility. Moreover, such measurements lead to erroneous conclusions in the presence of the type of inhomogeneities expected to characterize low-grade silicon. A direct determination

---

*The original research upon which this section is based was performed under previous HDL contracts (DAAG39-73-C-0171 and DAAG39-69-C-0039). The review of that work given here was prepared during the present contract period and presented at the 1978 Scanning Electron Microscopy Symposium.

of minority-carrier drift mobility would therefore be of interest. In the technique discussed here, both diffusion length and drift mobility may be determined.

Another problem to which the present methods are applicable is the degradation of bipolar transistors under energetic neutron bombardment. In the case of microwave (narrow basewidth) transistors, for example, decrease in drift mobility with fluence may be determinative. This occurs at such high fluences that the diffusion length will have degraded to the order of a few μm, requiring the determination of transport properties within spatial resolution of this order.

The conventional method of measuring the drift mobility is the Haynes-Shockley[63] technique in which the transport time of a pulse of minority carriers is monitored under application of a known field. The degradation of drift mobility in germanium under neutron bombardment has been studied in this manner.[64] The method is difficult to implement for material of short diffusion length, however, and the alternative approach proposed here, which may be regarded as a cw-equivalent of the above pulse technique, is more suitable to this case. A modulated SEM beam is employed as a source of minority carriers and a planar junction as a collector of these carriers. Injected carriers are swept toward or away from the junction by means of an applied field and changes in signal delay per unit field are used to derive the mobility.

Since the above technique requires special sample geometries and unusual experimental facilities, it is not likely to find wide application. Comparison of the above method was therefore made with field-free methods of determining the drift mobility which could readily be performed elsewhere. These methods are based on the frequency dependence of the observed diffusion length and measurement of the diffusion velocity. Such measurements yield both the diffusion length (L) and the lifetime (τ), which are related by the equation

$$L = \sqrt{D\tau} , \qquad (1)$$

---

[63] J.R. Haynes and W. Shockley, Phys. Rev. 81, 835 (1951).

[64] A.A. El-Difrawi, T.H. Yeh, and J.E. Christopher, J. Appl. Phys. 47, 272 (1976).

where D is the diffusivity. The mobility (μ) and diffusivity are in turn related by the Einstein relation

$$eD = \mu kT. \tag{2}$$

Approximate agreement among these various methods was found, and on this basis an experimental procedure is given here for the measurement of both the bulk diffusion length and the drift mobility.

6.2 EXPERIMENTAL PROCEDURE

The measurement of drift mobility was performed using a Jeol JSM-2 scanning electron microscope modified to permit intensity-modulation of the beam by deflection past an aperture. Signal recovery of the phase and amplitude information was by means of a network analyzer. The experimental design is illustrated schematically in Figure 64. A signal generator (HP8601) furnished the deflection signal as well as a phase and amplitude reference for the network analyzer (HP8407), permitting

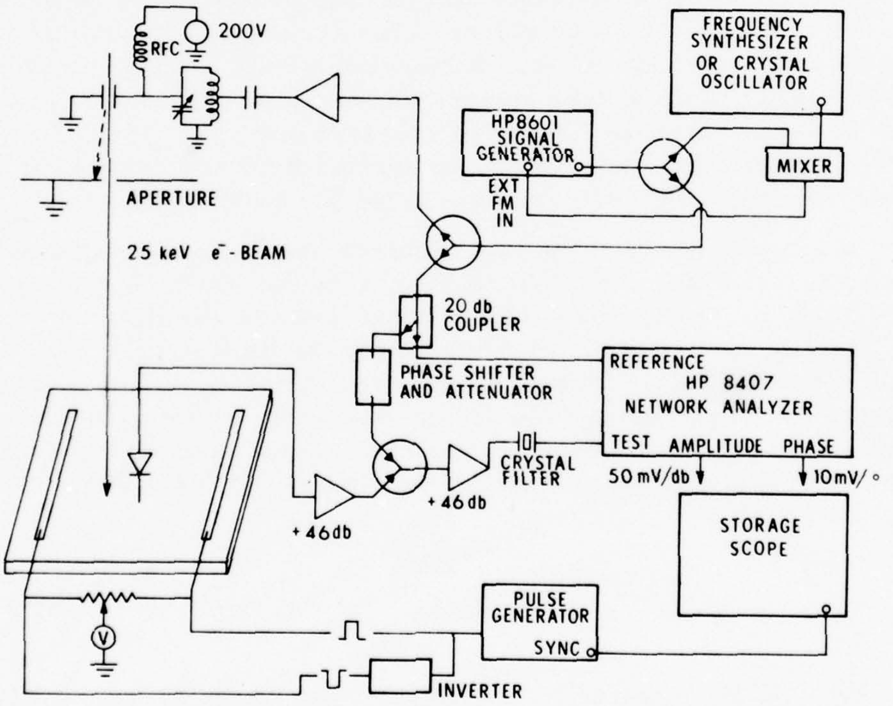

Figure 64. Schematic diagram of apparatus for narrowband signal recovery of the modulated beam response in amplitude and phase.

measurements in the range of 100 kHz to 110 MHz. The deflection signal is amplified by a 0.5W broadband amplifier and applied to a resonant deflection structure. A dc bias is also applied to the deflection plates to yield 50% duty cycle. The deflection plates are 0.5 x 2-in. microstrip substrates placed in the drift space beneath the anode. They were placed as far apart as possible to minimize interference with the beam. Deflection to cut off a 25-kV beam therefore requires some 200 volts. The plates are permanently left in place and do not interfere with conventional operation of the SEM.

The sample holder was provided with a MOSFET preamplifier of 46 dB gain and the sample stage furnished with minature 50-Ω coax to the chamber wall. Further amplification is provided outside of the SEM. To increase the dynamic range beyond the limit imposed by the 10-kHz noise bandwidth of the network analyzer, a crystal filter was interposed to yield a 10-Hz noise bandwidth. This introduced a phase slope of 90° between 3-dB points, necessitating the frequency stabilization of the signal generator, which was characterized by 100 Hz of incidental frequency modulation. A crystal-stabilized oscillator was used to phase-lock the signal generator. Resultant phase noise was then on the order of 0.3°. (Network analyzers are now available with receiver bandwidths of 10 Hz, which obviates this complication.)

With the sensitivity afforded by the crystal filter, it was found that residual pickup limited the dynamic range. In excess of 200 dB of isolation was required between the drive and output circuitry. The residual pickup was simply cancelled by means of a signal derived from the generator, suitably phase-shifted and attenuated. The phase and amplitude were iteratively adjusted to minimize the amplitude of the observed signal and to obtain a random phase characteristic of pure noise, while the beam current was turned off.

Application of the drift field to the sample was by means of a pulse generator and inverter, which could be adjusted to yield a balanced waveform at the junction position. A small (several kT/e) reverse bias was applied to the junction to reduce the junction capacitance and to make it a more ideal "sink" for minority carriers, insensitive to small bias transients. A typical sample is illustrated in Figure 65. The 3 Ω-cm phosphorus-doped chip is furnished with two large electrodes for application of the field, and with six diffused junctions (of 1-μm depth) in the central area. Two of the junctions are 1-mil x 20-mil (under the long metallization

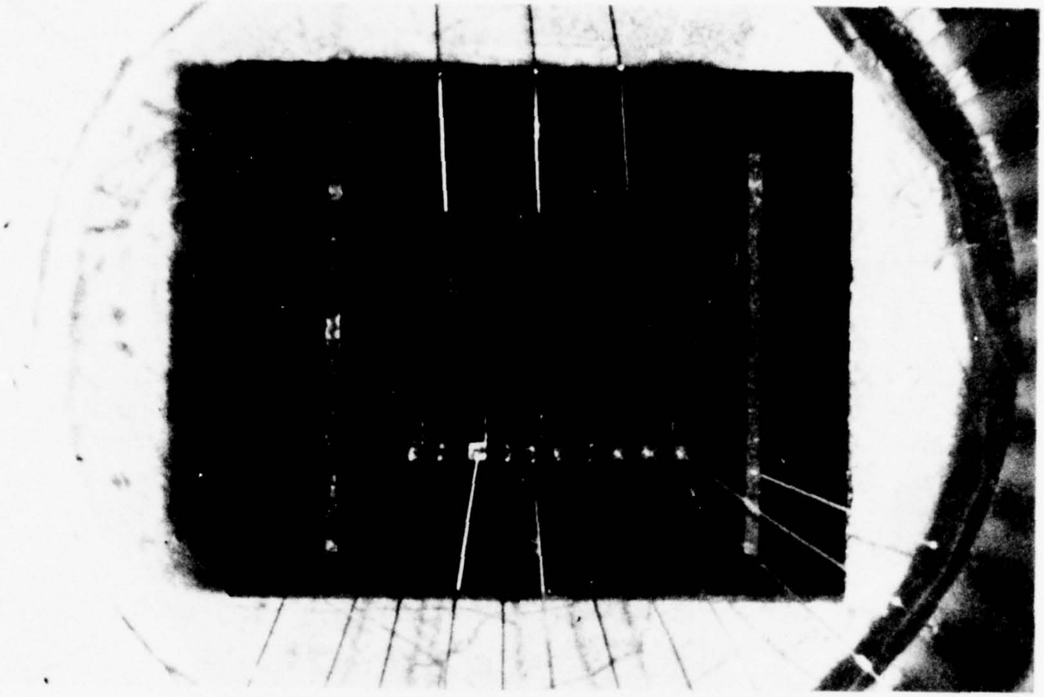

Figure 65. Silicon chip mounted on LSI package for mobility measurement.

fingers), and four are 1-mil x 1-mil (at the ends of the intermediate-length fingers). Seven ohmic contacts are provided at the ends of the small fingers for potential profiling. One of the bonding pads is furnished with small fingers for calibration of the magnification factor. The chip is mounted on the insulated substrate of an integrated circuit package.

6.3 EXPERIMENTAL RESULTS

Preliminary to the determination of mobility, the diffusion length was measured under ac-excitation conditions by recording the amplitude response as the beam was swept in a direction normal to the junction periphery. Modulation frequencies ranged from 30 kHz to 10 MHz. (The 30-kHz data were taken with an Ithaco 353 logarithmic phase-sensitive detector.) Data obtained at 1 MHz are illustrated in Figure 66 where results are shown for a sweep across one of the junctions. The phase response is also

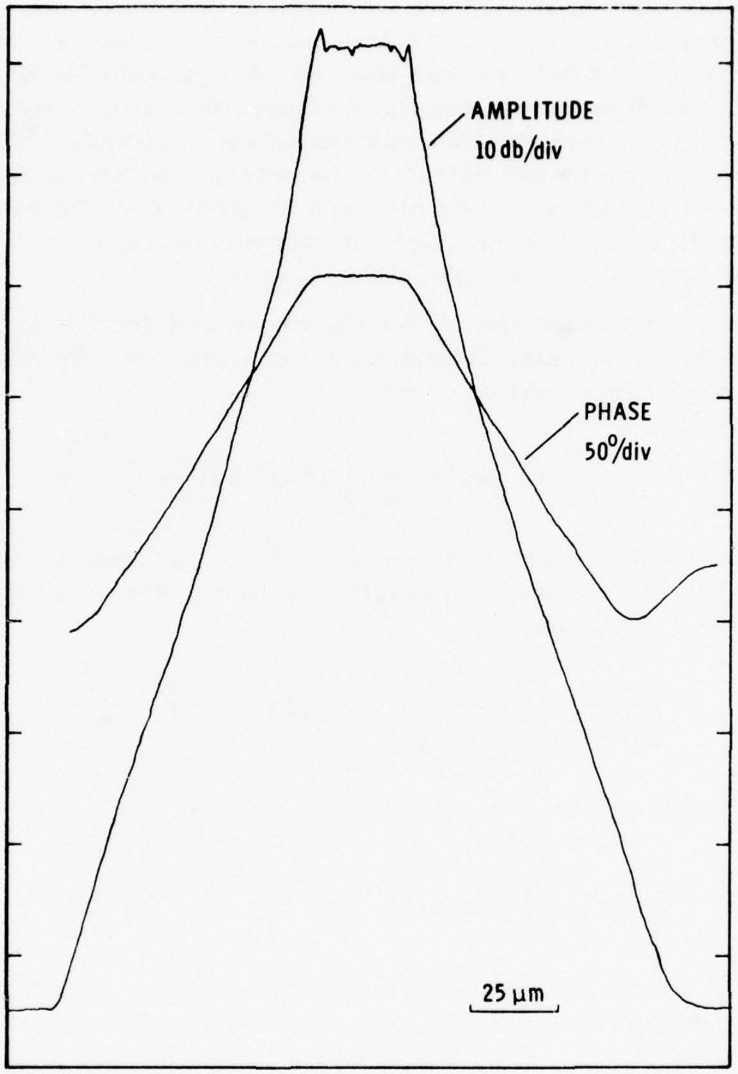

Figure 66. Amplitude and phase response to a 1-MHz modulated beam as the beam is scanned in a direction normal to the junction peripheries.

given. A 25-keV beam was used. This energy represented a compromise between considerations of ease of deflection and depth of penetration, which governs the imporance of surface effects. Beam current was held to less than 30 pA to minimize the volume over which high-injection conditions prevailed (i.e., where the excess carrier concentration was sufficient to modulate the local conductivity). Since the pair creation energy in silicon is approximately 3.65 eV, each 25-keV electron generates on the order of 7000 carrier pairs, so that high-injection conditions certainly prevail within the energy deposition volume.

An analytical expression for the phase and amplitude response for excitation at angular frequency ω has been given by McKelvey for the one-dimensional case:[65]

$$V(x, \omega) = V(0, \omega) \exp\left(-\frac{x}{L(\omega)}\right) \exp\left(-i \frac{x}{L(0)} \gamma(\omega)\right), \qquad (3)$$

where x is the distance of the point of injection from the junction. Here $L(\omega)$ is the ac diffusion length, related to the dc diffusion length $L(0)$ by the equation

$$\frac{L(\omega)}{L(0)} = \left\{\frac{1}{2}\left[1 + \left(1 + (\omega\tau)^2\right)^{1/2}\right]\right\}^{-1/2} \qquad (4)$$

and $\gamma(\omega)$ is the phase factor given by

$$\gamma(\omega) = \left\{\frac{1}{2}\left[-1 + 1\left(+ (\omega\tau)^2\right)^{1/2}\right]\right\}^{+1/2}. \qquad (5)$$

The amplitude function thus yields the ac diffusion length directly. The data of Figure 66 exhibit some variation in the apparent local diffusion length and this is due to deviations from one-dimensional behavior near the junction, as well as to the effects of surface recombination. With increasing distance from the junction, the diffusion length approaches the bulk value. The effects of surface recombination have been treated analytically by vanRoosbroeck,[66] and are calculable in principle. However, explicit fitting of the

---

[65] J.P. McKelvey, Solid State and Semiconductor Physics (Harper and Row, 1966, New York), pp. 439-440.

[66] W. vanRoosbroeck, J. Appl. Phys. 26, 380 (1955).

amplitude function, taking into account surface effects and detector geometry, is deemed to be intractable. vanRoosbroeck has shown that at distances from the junction sufficiently great, surface recombination affects the amplitude only as a multiplicative constant. It is therefore preferable, when possible, to take the experimental approach of providing sufficient dynamic range to yield the bulk value of diffusion length directly. A first-order correction for deviation from one-dimensional geometry was made (discussed below) and a value of 10.9 μm for the diffusion length obtained. The noise level of Figure 66 corresponds to about 4 dB above thermal noise. The phase characteristic has a range of 150° before noise dominates and indicates a uniform signal propagation velocity. Measurements of the kind shown in Figure 66 have previously been made on germanium by Munakata,[67] at lower frequencies and for longer diffusion lengths, in order to verify the applicability of the one-dimensional model. Consistency within experimental error was observed.

The drift mobility is derived most directly from the change in signal propagation velocity v, as observed from the change in phase (ϕ) under application of an electric field (E). We have then

$$\mu = \frac{v_{drift}}{E} = \frac{1}{E}(v_E - v_0) = \frac{\omega x}{E}\left(\frac{1}{\phi_E(x)} - \frac{1}{\phi_0(x)}\right). \tag{6}$$

v_0 is governed strictly by diffusion whereas v_E has the drift velocity superimposed on it. Field strengths were as high as 30 to 50 V/cm and short pulses were employed to minimize sample heating. Use of the crystal filter, however, limited the signal bandwidth to such an extent that the phase did not settle within the desired pulse lengths. Equivalent information was therefore derived from the amplitude function. Figure 67 shows the amplitude profiles under zero field as well as under retarding and accelerating fields. Analysis assumes that equal amplitude signals correspond to equal propagation times. Thus,

$$\mu = \frac{1}{E}(v_E - v_0) = \frac{v_0}{E}\left(\frac{x_E}{x_0} - 1\right), \tag{7}$$

---

[67] C. Munakata and T.E. Everhart, Japan J. Appl. Phys. 11, 913 (1972).

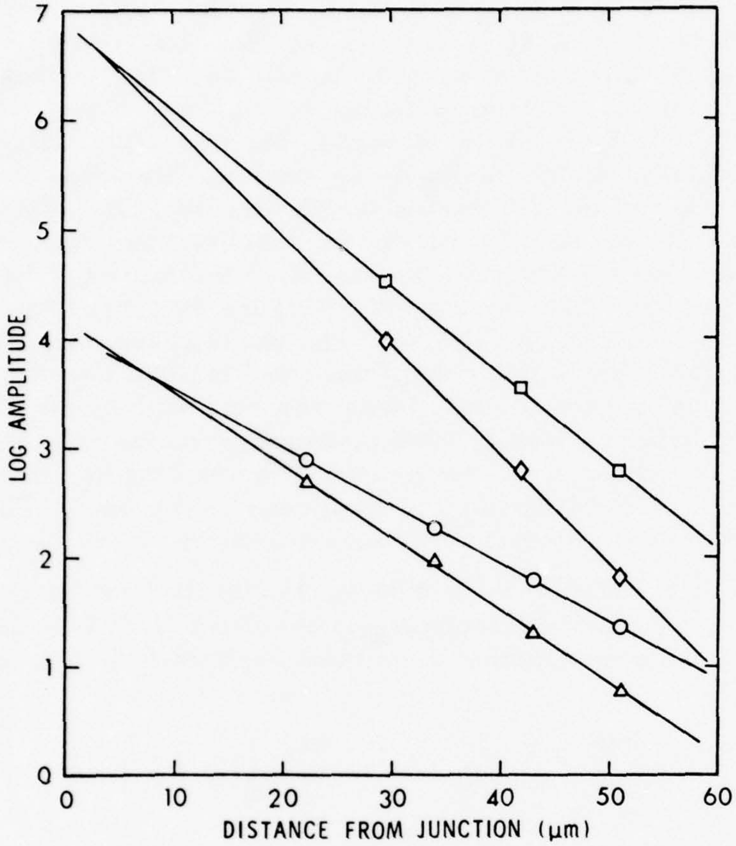

Figure 67. The dependence of amplitude on distance from the junction under field-free (△, □) conditions, as well as accelerating pulsed field (○), and retarding pulsed field (◇) conditions, for a 1-MHz modulated beam. The applied field was 11 V/cm. The corresponding sets of curves have been separated vertically for clarity, so the amplitude scale is arbitrary.

where x_E and x_0 refer to equal-amplitude coordinates on the respective curves. Mobilities determined in this manner were 250 cm^2/V-sec and 270 cm^2/V-sec on the two sides of the junction. The curves shown in the figure should intersect at the junction periphery and the deviation may be due to conductivity modulation near the point of injection.

Mobilities were also measured using phase information, without the crystal filter. Typical values were consistent with those found above, centering about 240 cm^2/V-sec. These values are low compared to the mobility of about 450 cm^2/V-sec expected for holes in 3 Ω-cm n-type material. (Possible reasons for the discrepancy will be discussed below.) The finding of an unexpected low mobility motivated a comparison with other, field-free, methods of determining the mobility.

The mobility may be determined from the diffusivity using the Einstein relationship [Eq. (2)] if both the lifetime and diffusion length are known. Both of these quantities may be determined from measurement of $L(\omega)$ or the signal propagation velocity at a number of frequencies, encompassing such frequencies that $\omega\tau >> 1$. (See Eqs. (4) and (5).) We have obtained a mobility value by comparison of the 1-MHz diffusion length with the dc value, as well as by measurement of the signal propagation velocity for a wide range of frequencies.

Results for the measurement of the dc diffusion length are shown in Figure 68. The experimental method for this measurement has been described elsewhere.[68] Since the noise limit of the method is imposed by the 1/f-noise of the (unpassivated) detector junction, dynamic range equivalent to that of the ac measurement is obtained by means of signal averaging. The noise level in this measurement is on the order of a few pA. The amplitude function is qualitatively similar to that of Figure 66 in that the apparent diffusion length is foreshortened near the junction, due to surface effects and geometric factors, and approaches a constant value at some distance from the junction. Since the apparent diffusion length is spatially varying, an improvement on a one-dimensional treatment is desirable. The steady-state solution of the diffusion equation in spherical coordinates, for point source excitation, is given by

$$n(r) = \frac{A}{r} \exp(-r/L) , \qquad (8)$$

where n is the concentration at distance r from the source and A is an assumed source strength. The measured signal is directly proportional to the value of n at the junction. A fit of the functional form $(1/x) \exp(-x/L)$ to the data yielded a spatially invariant value of diffusion length of 17.6 μm, which was taken to be the bulk value. The same considerations apply to the 1-MHz data. Verification that the data for the two cases are analogous is provided in a log-log

---

[68] S. Othmer and O.L. Curtis, Jr., IEEE Trans. Nucl. Sci. 20, 204 (Dec. 1973).

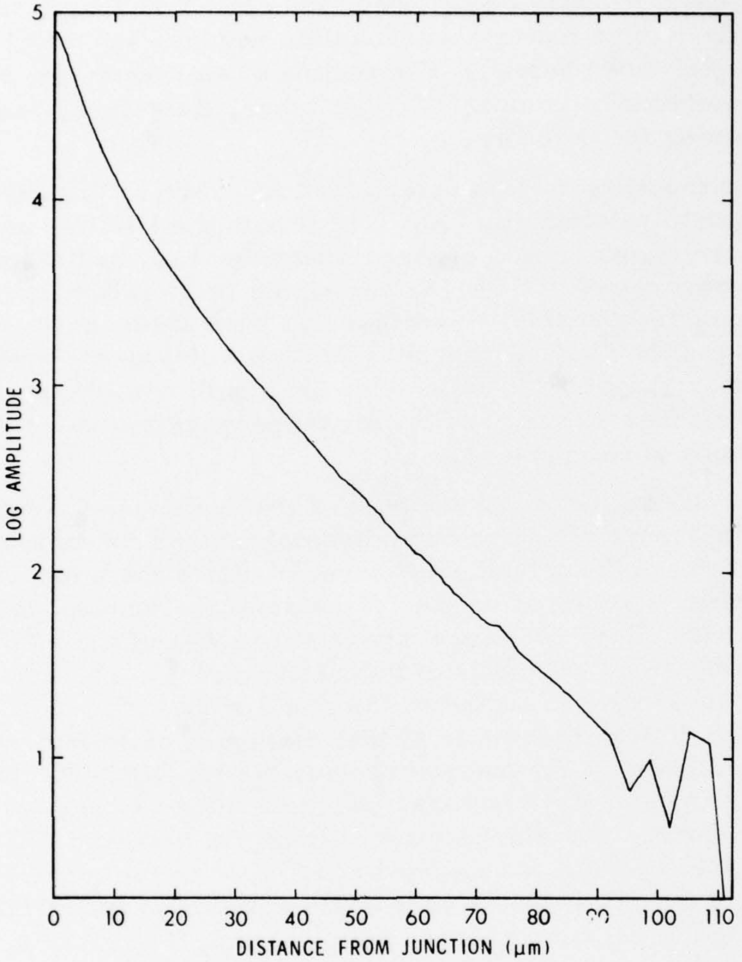

Figure 68. Measurement of the minority-carrier current as a function of distance from the point of injection to the junction, for the determination of the dc diffusion length. Shown is the output of a multichannel scaler after summation of traces for signal-to-noise enhancement. The amplitude scale is arbitrary.

plot of the amplitude function, shown in Figure 69. The data sets have been superimposed by translation along the two coordinate axes, and the correspondence demonstrates that the only difference between them is the spatial scale (i.e., the bulk diffusion length). The same functional form was therefore used to fit these data and the value of 10.9 μm already referred to was obtained. Using Eq. (4),

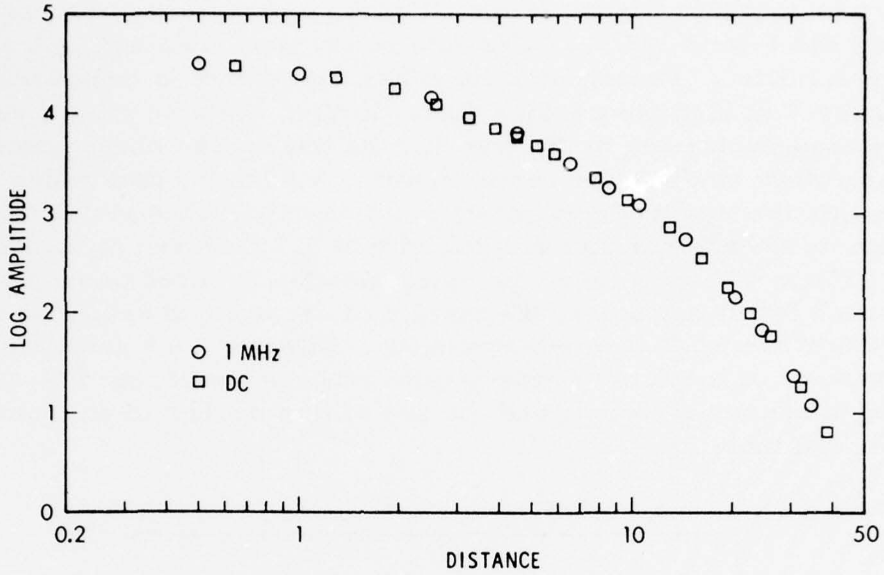

Figure 69. Comparison of the dc diffusion length and the 1-MHz diffusion length. The scales are arbitrary and the curves have been displaced along the coordinate axes for superposition.

the lifetime is determined to be 640 ns, the diffusivity 4.84 cm^2/sec, and the mobility 190 cm^2/V-sec. The precision of this value is poor, due to the use of the rather low frequency of 1 MHz for this short lifetime ($\omega\tau = 4$). An error of 10% in the 1-MHz diffusion length implies an error of some 26% in mobility in this case. Nevertheless, the low values of mobility found above with application of an electric field stand confirmed to within the accuracy of this determination.

The second field-free method of determining the drift velocity is based on phase measurements of the signal propagation velocity. The phase shift in Eq. (3) has the form $\gamma x/L(0)$, so that the signal propagation velocity is

$$v = L(0)\ (\omega/\gamma), \tag{9}$$

from which the lifetime may be determined if the dc diffusion length is also known. The signal propagation velocity is closely related to the diffusion velocity, given by $L(0)/\tau$. In the low-frequency limit, the signal propagation is equal to twice the diffusion velocity. The data obtained for signal propagation velocity are shown in Figure 70 for all of the measurement frequencies. Only the 1-MHz and 3.6-MHz data points were obtained with a crystal filter. Precision of the other data points is considerably poorer – at high frequencies due to limited dynamic range, and at low frequencies due to the fact that the total phase change measured was rather small. The curve shown is a fit to the data which weights the two best data points most heavily. This yields a lifetime of 320 ns, and thus a diffusivity of 9.7 cm^2/sec or a mobility of 370 cm^2/V-sec. Since the determination is based on data taken at such low frequencies, the margin of error could easily be +100/-70 cm^2/V-sec in this determination. However, the general conformance of the data to expectations tends to justify the use of a one-dimensional model, and the use of this method of determining the drift mobility.

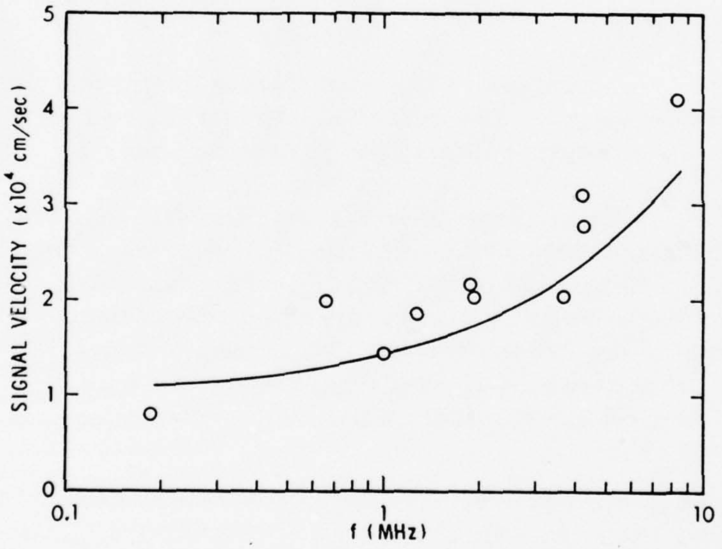

Figure 70. Plot of signal propagation velocity, determined from phase measurements, vs modulation frequency. The fit shown is based on the one-dimensional model. Refer to the text for discussion of the fit.

6.4 DISCUSSION

Comparison has been made between methods of determining drift mobility which do not require application of a field and those using a pulsed electric field. The data are recapitulated in Table 5. Considerable spread in the measured values was found among the various techniques, but a general tendency for the values to be low compared to expectations was manifested. This is surprising, and several possible explanations have been considered. First, under high-injection conditions, transport is governed not by the drift mobility, but rather by the ambipolar mobility, which tends to zero in the intrinsic limit. At the low beam currents employed here, such high-injection conditions were determined to exist only within the energy deposition volume. Therefore, it is unlikely that this factor is principally responsible for the observation of a low mobility. Moreover, the field-free methods are governed under high-injection conditions by the ambipolar diffusivity, which does not vanish in the intrinsic limit, and is, in fact, larger than the low-injection hole diffusivity in the case of n-type samples. A second possible explanation is that the mobility is reduced due to local heating, but this factor has likewise been found insufficient to explain the observed discrepancy. Finally, it is conceivable that the present measurements are inordinately influenced by the presence of the surface. An upper limit to the possible influence of the surface is indicated by the channel mobilities

Table 5.

Mobilities Determined by Various Methods

Measurement Technique	Mobility (cm^2/V-sec)
Pulsed Field, Amplitude Function	250-270
Pulsed Field, Phase Function	240
ac-Diffusion Length	190
Signal Velocity	370
(Expected Value)	(450)

of MOS transistors, where transport is influenced by the interface and in which mobilities on the order of one-half of bulk mobilities are observed. This effect would seem to be insufficient to explain the discrepancy in the present case, which approaches the conditions for a bulk measurement much more closely.

The spread in the observed mobility values among the various techniques is ascribed principally to the nonoptimal choice of operating frequencies in the case of the field-free techniques, and to the fact that mobility determinations become vastly more difficult at short diffusion lengths. Radiation effects studies at such short diffusion lengths therefore appear to be unattractive. On the other hand, the prospect of using these methods for the characterization of solar cells appears promising. Silicon solar cells must exhibit diffusion lengths of at least 50 μm in order to have any prospect of economic viability and the above techniques should be capable of yielding good mobility values in the range of diffusion lengths above 20 μm.

The principal shortcomings of the above techniques relate to the influence of the surface on the measurements and the assumption of one-dimensional character of transport. Both of these liabilities are remedied if measurements of the ac diffusion length are made with a bevel geometry,[69] in which the bombarded surface and the collecting surface form a wedge of arbitrary apex angle (on the order of 10°). Transport then occurs through the bulk and the effect of the surface on the measurements is totally negligible as long as the surface recombination velocity at the injecting surface is uniform. The transport is also more one-dimensional in character by virtue of the fact that the diffusion front is tangential to the collecting surface. DC measurements of diffusion length by such methods have been quite common, particularly for GaAs. The simple expedient of measuring the amplitude and phase response using two appropriate frequencies should yield both the dc diffusion length and the drift mobility for the material as well as a measure of the spatial uniformity of these parameters. One frequency should be chosen such that $\omega\tau \ll 1$, to yield a diffusion length close to the dc value, and the other should be chosen such that $\omega\tau > 10$, to give values for the lifetime on the basis of both the phase and the amplitude response. Jointly, then, these parameters yield the mobility. The determination of good mobility values by this method requires

---

[69] W.H. Hackett, Jr., J. Appl. Phys. 43, 1649 (1972).

precision not usually associated with diffusion length measurements. We have used the bevel geometry for determining diffusion lengths of 40 μm on solar cells with 5% precision, and have found agreement of this value with a short-circuit current measurement of the diffusion length using the uniform generation of a Cobalt-60 gamma source. Measurement with the bevel geometry clearly does afford the desired accuracy.

LITERATURE CITED

1. R.A. Williams and R. D. Nelson, IEEE Trans. Nucl. Sci. 22, 2639 (1975).
2. G.A. Hartsell, in "Proceedings of the 1975 International Conference on the Application of CCDs," San Diego, CA, Oct. 1975.
3. J.E. Carnes, A.D. Cope, and L.R. Rockett, Final Report on Contract F19628-75-C-0121, September 1976 (RADC-TR-76-285).
4. N.S. Saks, J.M. Killiany, and W.D. Baker, in "Proceedings of NASA-JPL Conference on CCD Technology and Applications," Washington, D.C., Dec. 1976.
5. C.P. Chang and K. G. Aubuchon, Final Report on Contract N00173-76-C-0166, March 1977.
6. N.S. Saks, IEEE Trans. Nucl. Sci. 24, 2153 (1977).
7. D.K. Schroder and H.C. Nathanson, Solid-State Electronics 13, 577 (1970).
8. R.F. Pierret and D.W. Small, IEEE Trans. Electron Devices 20, 457 (1973).
9. D.W. Small and R.F. Pierret, Solid-State Electronics 19, 505 (1976).
10. T. Takino, Ph.D. thesis, UCLA 1976.
11. P. Tomanek, Solid-State Electronics 12, 301 (1969).
12. P.U. Calzolari, S. Graffi, and C. Morandi, Solid-State Electronics 20, 205 (1977).
13. M. Zerbst, Z. Angew. Phys. 22, 30 (1966).
14. D.K. Schroder and J. Guldberg, Solid-State Electronics 14, 1285 (1971).
15. J.G. Simmons and L.S. Wei, Solid-State Electronics 19, 153 (1976).
16. A. Many, Y. Goldstein, and N.B. Grover, Semiconductor Surfaces (North-Holland, Amsterdam, 1965), pp. 194-208.

17. R.F. Pierret and R.J. Grossman, Solid-State Electronics 20, 373 (1977).

18. P.S. Winokur, H.E. Boesch, Jr., J.M. McGarrity, and F.B. McLean, IEEE Trans. Nucl. Sci. 24, 2113 (1977).

19. F.P. Heiman, IEEE Trans. Electron Devices 14, 781 (1967).

20. J.L. Moll, Physics of Semiconductors (McGraw-Hill, New York, 1964), p. 118; A.S. Grove, Physics and Technology of Semiconductor Devices (Wiley, New York, 1967), p. 174.

21. O.L. Curtis, Jr., IEEE Trans. Nucl. Sci. 13, 33 (Dec. 1966).

22. J.R. Srour, IEEE Trans. Nucl. Sci. 20, 190 (Dec. 1973).

23. F.B. McLean, H.E. Boesch, Jr., and J.M. McGarrity, IEEE Trans. Nucl. Sci. 23, 1506 (1976).

24. B.L. Gregory, IEEE Trans. Nucl. Sci. 16, 53 (Dec. 1969).

25. O.L. Curtis, Jr., J. Appl. Phys. 39, 3109 (1968).

26. O.L. Curtis, Jr., and J.R. Srour, IEEE Trans. Nucl. Sci. 20, 196 (Dec. 1973).

27. C.P. Chang, IEEE Trans. Nucl. Sci. 24, 2190 (1977).

28. C.H. Sequin and M.F. Tompsett, Charge Transfer Devices (Academic Press, New York, 1975), p. 134.

29. M. Nakagiri, Jap. J. Appl. Phys. 13, 1610 (1974).

30. K.O. Jeppson and C.M. Svensson, J. Appl. Phys. 48, 2004 (1977).

31. A. Goetzberger and H.E. Nigh, Proc. IEEE 54, 1454 (1966).

32. B.E. Deal, M. Sklar, A.S. Grove, and E.H. Snow, J. Electrochem Soc. 114, 266 (1967).

33. A. Goetzberger, A.D. Lopez, and R. J. Strain, J. Electrochem Soc. 120, 90 (1973).

34. I. Kobayashi, M. Nakahara, and M. Atsumi, Proc. IEEE 61, 249 (1973).

35. D. Neamen, W. Shedd, and B. Buchanan, IEEE Trans. Nucl. Sci. 21, 211 (Dec. 1974).

36. R.A. Kjar and J. Peel, IEEE Trans. Nucl. Sci. 21, 208 (Dec. 1974).

37. K.M. Schlesier, IEEE Trans. Nucl. Sci. 21, 152 (Dec. 1974).

38. E. Harari, Appl. Phys. Letters 29, 25 (1976).

39. E. Harari and D.J. McGreivy, IEEE Trans. Electron Devices 24, 1277 (1977).

40. J.R. Brews, J. Appl. Phys. 46, 2181 (1975); 46, 2193 (1975).

41. J.T.C. Chen and R.S. Muller, J. Appl. Phys. 45, 828 (1974).

42. A.A. Guzev, G.L. Kurishev, and S.P. Sinitsa, Phys. Status Solidi A14, 41 (1972).

43. T.E. Everhart and P.H. Hoff, J. Appl. Phys. 42, 5837 (1971).

44. R.A. Kjar and G. Kinoshita, IEEE Trans. Nucl. Sci. 20, 315 (Dec. 1973).

45. J.R. Srour, O.L. Curtis, Jr., and K.Y. Chiu, IEEE Trans. Nucl. Sci. 21, 73 (Dec. 1974).

46. J.L. Peel et al., IEEE Trans. Nucl. Sci. 22, 2185 (1975).

47. S.T. Wang and B.S.H. Royce, IEEE Trans. Nucl. Sci. 23, 1586 (1976).

48. R.A. Williams et al., AFCRL-TR-75-0320, May 1975.

49. D.H. Habing and B.D. Shafer, IEEE Trans. Nucl. Sci. 20, 307 (Dec. 1973).

50. E.P. EerNisse and G.F. Derbenwick, IEEE Trans. Nucl. Sci. 23, 1534 (1976).

51. R.L. Nielsen and D.K. Nichols, IEEE Trans. Nucl. Sci. 20, 319 (Dec. 1973).

52. E. Harari, S. Wang, and B.S.H. Royce, J. Appl. Phys. 46, 1310 (1975).

53. H.H. Sander and B.L. Gregory, IEEE Trans. Nucl. Sci. 22, 2157 (1975).

54. H.E. Boesch, Jr., F.B. McLean, J.M. McGarrity, and G.A. Ausman, Jr., IEEE Trans. Nucl. Sci. 22, 2163 (1975).

55. J.R. Srour, S. Othmer, O.L. Curtis, Jr., and K.Y. Chiu, IEEE Trans. Nucl. Sci. 23, 1513 (1976).

56. H.E. Boesch, Jr., and J.M. McGarrity, IEEE Trans. Nucl. Sci. 23, 1520 (1975).

57. H.E. Boesch, Jr., IEEE Trans. Nucl. Sci. 24, 2135 (1977).

58. G.F. Derbenwick and B.L. Gregory, IEEE Trans. Nucl. Sci. 22, 2151 (1975).

59. K.G. Aubuchon, IEEE Trans. Nucl. Sci. 18, 117 (Dec. 1971).

60. R.C. Hughes, IEEE Trans. Nucl. Sci. 18, 281 (Dec. 1971).

61. O.L. Curtis, Jr., and J.R. Srour, J. Appl. Phys. 48, 3819 (1977).

62. O.L. Curtis, Jr., and J. R. Srour, and K.Y. Chiu, IEEE Trans. Nucl. Sci. 22, 2174 (1975).

63. J. R. Haynes and W. Shockley, Phys. Rev. 81, 835 (1951).

64. A.A. El-Difrawi, T.H. Yeh, and J.E. Christopher, J. Appl. Phys. 47, 272 (1976).

65. J.P. McKelvey, Solid State and Semiconductor Physics (Harper and Row, 1966, New York), pp. 439-440.

66. W. VanRoosebroeck, J. Appl. Phys. 26, 380, (1955).

67. C. Munakata and T.E. Everhart, Japan J. Appl. Phys. 11, 913 (1972).

68. S. Othmer and O.L. Curtis, Jr., IEEE Trans. Nucl. Sci. 20 , 204 (Dec. 1973).

69. W. H. Hackett, Jr., J. Appl. Phys. 43, 1649 (1972).

(This page intentionally left blank.)

DISTRIBUTION LIST

Commander
U. S. Army Material & Mechanics
Research Center
Watertown, MA 02172
Attn: DRXMR-HH, J. Dignam

Commander
U.S. Army Missile R&D Command
Redstone Arsenal, AL 35809
Attn: DRCPM-LCEV, H.Henriksen
DRSMI-RGD, V. Ruwe
DRCPM-PE-EA, W. Wagner

Commander
U.S. Army Mobility Equipment
R&D Command
Fort Belvoir, VA 22060
Attn: DRDME-E, J. Bond, Jr.

Commander
U.S. Army Night Vision Lab
Fort Belvoir, VA 22060
Attn: DRSEL-NV-SD, A. Parker
J. Pollard

Commander
U.S. Army Test & Eval Command
Aberdeen Proving Ground, MD
Attn: DRSTE-FA 21005
DRSTE-EL, R. Kolchin
DRSTE-EL

Director
U.S. Army TRADOC Systems
Analysis Activity
White Sands Missile Range, NM
Attn: O. Miller 88002

Commander
U.S. Army Training &
Doctrine Command
Fort Monroe, VA 23651
Attn: ATORI-OP-SW

Project Manager
XM-1 Tank System
Department of the Army
28150 Dequindre
Warren, MI 48092
Attn: DRCPM-GCM-SW

Commander
Naval Air Systems Command
Washington, DC 21360
Attn: AIR 350F
AIR 5324K
AIR 310

Commander
Naval Electronic Systems Command
Washington, DC 20360
Attn: NAVELEX 51024, C.Watkins

Commanding Officer
Naval Intelligence Support Ctr
4301 Suitland Rd., Bldg 5
Washington, DC 20390
Attn: NISC Library

Commander
Naval Ocean Systems Center
San Diego, CA 92152
Attn: Code 4471 (Tech Lib)

Superintendent
Naval Postgraduate School
Monterey, CA 93940
Attn: Code 2124, Tech Repts Libr.

Director
Naval Research Laboratory
Washington, DC 20375
Attn: Code 7750, J. Boris
Code 5216, H. Hughes
Code 6444
Code 6624, J. Ritter
Code 5580, G. Sigel
Code 6601, E. Wolicki
Code 2627
Code 4104
Code 5210
Code 6701
Code 5216
W.D. Baker

Commander
Naval Sea Systems Command
Washington, DC 20362
Attn: SEA-9931, S. Barham
SEA-04531

Officer-in-Charge
Naval Surface Weapons Center
White Oak, Silver Spring, MD 20910
Attn: Code F31
Code F30

Commander
Naval Surface Weapons Center
Dahlgren Laboratory
Dahlgren, VA 22448
Attn: DG-50, W. Holt

Commander
Naval Weapons Center
China Lake, CA 93555
Attn: Code 533, Tech. Lib.

Commanding Officer
Nuclear Weapons Tng Center Pacific
Department of the Navy
Naval Air Station, North Island
San Diego, CA 92135
Attn: Code 32

Office of Naval Research
Arlington, VA 22217
Attn: Code 427
Code 421, Doran W. Padgett

Director
Strategic Systems Project Office
Department of the Navy
Washington, DC 20376
Attn: NSP-2342, Richard L. Coleman
NSP-2701, J. Pitsenberger
NSP-230, D. Gold
NSP-27334, B. Hahn

Commander
Aeronautical Systems Division, AFSC
Wright-Patterson AFB, OH 45333
Attn: ASD(YS)
ENACC, R. Fish
ASD/ENESS, P. Marth

Air Force Aero-Propulsion Laboratory
Wright-Patterson AFB, OH 45433
Attn: POE-2, J. Wise

Air Force Avionics Laboratory
Wright-Patterson AFB, OH 45433
Attn: DHE, H. Hennecke
DH, LTC McKenzie
AAT, Mason Friar
DHE-2

Air Force Institute of Technology,
Air University
Wright-Patterson AFB, OH 45433
Attn: ENP, Chas. J. Bridgman

Headquarters
Air Force Systems Command
Andrews AFB
Washington, DC 20334
Attn: DLCA

Air Force Weapons Laboratory
Kirtland AFB, NM 87117
Attn: ELP, TREE Section
ELA
ELXT
EL, C. Baum
ELS
NXS
J. Mullis
NT
SUL
DEX
R. Maier

Headquarters
Electronic Systems Division/IN
Department of the Air Force
Hanscom AFB, MA 01731
Attn: INDC/21

Headquarters
Electronic Systems Division/YSEA
Department of the Air Force
Hanscom AFB, MA 01731
Attn: YSEA

Assistant to the Secretary of
Defense
Atomic Energy
Washington, DC 20301
Attn: Executive Assistant

Director
Command & Control Tech Center
Department of Defense
The Pentagon, Rm BE 685
Washington, DC 20301
Attn: C-362, Mr. Adkins

Defense Communication Engineer
Center
1860 Wiehle Avenue
Reston, VA 22090
Attn: Code R410

Defense Documentation Center
Cameron Station
Alexandria, VA 22314
Attn: DD (12)
DDC-TCA (2)

Commander
Defense Electronic Supply Center
1507 Wilmington Pike
Dayton, OH 45401
(Thru DSA for CNWDI)
Attn: DESC-ECS

Director
Defense Intelligence Agency
Washington, DC 20301
Attn: DB-4C

Director
Defense Nuclear Agency
Washington, DC 20305
Attn: STRA
STVL
RAEV
DDST
TITL (4)

Commander
Field Command
Defense Nuclear Agency
Kirtland AFB, NM 87115
Attn: FCPR

Director
Interservice Nuclear Weapons
School
Kirtland AFB, NM 87115
Attn: TTV

Director
Joint Strat TGT Planning Staff
Offutt AFB
Omaha, NB 68113
Attn: JLTW-2

Chief
Livermore Division Fld Command
DNA
Lawrence Livermore Laboratory
P.O. Box 808
Livermore, CA 94550
Attn: FCPRL

National Communications System
Office of the Manager
Department of Defense
Washington, DC 20305
Attn: NCS-TS, C. Bodson

Director
National Security Agency
Department of Defense
Fort George G. Meade, MD 20755
Attn: R-52, O. Van Gunten

Under Secy of Def for Research
& Engineering
Department of Defense
Washington, DC 20301
Attn: Strategic & Space Systems (OS)

Director
BMD Advanced Technology Center
Huntsville Office
Department of the Army
P.O. Box 1500
Huntsville, AL 35807
Attn: ATC-T
F. Hoke

Commander
BMD Systems Command
Department of the Army
P.O. Box 1500
Huntsville, AL 35807
Attn: BMDSC-TEN, N. Hurst
BMDSC-HEN

Commander
ERADCOM Technical Support Activity
Department of the Army
Fort Monmouth, NJ 07703
Attn: DRSEL-TL-EN
DRSEL-PL-ENV, H. Bomke
A. Cohen
DRSEL-TL-MD, G. Gaule
DRSEL-NL-RO, R. Brown

Commander
Fort Huachuca
Department of the Army
Fort Huachuca, AZ 85613
Attn: Tech Ref Div

Commander
Redstone Scientific Info Center
U.S. Army R&D Command
Redstone Arsenal, AL 35809
Attn: Chief, Documents (3)
DRDMI-TBD

Commander
Harry Diamond Laboratories
Department of the Army
2800 Powder Mill Road
Adelphi, MD 20783

Attn: J. Thompkins
DELHD-NP, F. Wimenitz
DELHD-NP
DRXDO-EM-1, J. Miletta
DELHD-EM, R. McCoskey
DELHD-RBA, J. Rosado
DELHD-RBG
DELHD-RBH, F. McLean (10)
DELHD-TF, R. Oswald, Jr.
DELHD-TI (Tech Lib) (3)
DELHD-RB, J. McGarrity
DELHD-TI (Tech Reports)
Chairman, Editorial Comm.
DRXDO-AS (Records)

Secretary of the Army
Washington, DC 20301
Attn: ODUSA or Daniel Willard

Commander
U.S. Army Armament Research &
Development Command
Dover, NJ 07801
Attn: DRDAR-LCN-F
DRDAR-LCA-PD
DRDAR-TSS No. 59

Director
U.S. Army Ballistic Research Labs
Aberdeen Proving Ground, MD 21005
Attn: DRDAR-BLT
DRXBR-AM, W. Vanantwerp
DRXRD-BVL, D. Rigotti
STEAP-RF, R. Harrison

Chief
U.S. Army Communications Sys Agcy
Fort Monmouth, NJ 07703
Attn: SCCM-AD-SV (Library)
CCM-RD-T, S.Krevsky

Commander-in-Chief
U.S. Army Europe & Seventh Army
APO New York 09403
(Heidelberg)
Attn: ODSCE-E AEAGE-PI

Commander
U.S. Army Intelligence & Sec Cmd
Arlington Hall Station
4000 Arlington Blvd.
Arlington, VA 22212
Attn: IARDA-OS, R. Burkhardt

Headquarters
Electronic Systems Division, AFSC
Hanscom AFB, MA 01731
Attn: Technical Library

Commander
Foreign Technology Division, AFSC
Wright-Patterson AFB, OH 45433
Attn: ETDP
ETDP, B. Ballard

Commander
Rome Air Development Center,
Griffiss AFB, NY 13441 AFSC
Attn: RADC/RBRP, C. Lane
RADC/RBRAC, I. L. Krulac

Commander
Rome Air Development Center,
Hanscom AFB, MA 01731 AFSC
Attn: ESR, B. Buchanan
ESE, A. Kahan
ETS, R. Dolan

Space & Missile Systems Organization/DY
Air Force Systems Command
P. O. Box 92960
Worldway Postal Center
Los Angeles, CA 90009
(Technology)
Attn: DYS

Space & Missile Systems Organization/IN
Air Force Systems Command
P. O. Box 92960
Worldway Postal Center
Los Angeles, CA 90009
(Intelligence)
Attn: IND

Space & Missile Systems Organization/MN
Air Force Systems Command
Norton AFB, CA 92409
(Minuteman)
Attn: MNNH
MNNG

Space & Missile Systems Organization/RS
Air Force Systems Command
P. O. Box 92960
Worldway Postal Center
Los Angeles, CA 90009
(Reentry Systems)
Attn: RSSE, LTC K. Gilbert
RSMA, Lt. D. Higgins
RSMG, Capt. Collier

Strategic Air Command/XPFS
Offutt AFB, , NB 68113
Attn: XPFS, M. Carra
NRI-STINFO Library

Space & Missile Systems Organization/SK
Air Force Systems Command
P. O. Box 92960
Worldway Postal Center
Los Angeles, CA 90009
(Space Comm Systems)
Attn: SKP, P. Stadler

Space & Missile Systems Organization/YA
Air Force Systems Command
P. O. Box 92960
Worldway Postal Center
Los Angeles, CA 90009
Attn: YAS

Director (INWS)
3416th Technical Training Squadron
Air Training Command
Department of the Air Force
Kirtland AFB, NM 87115
Attn: TTV

Department of Energy
Albuquerque Operations Office
P. O. Box 5400
Albuquerque, NM 87115
Attn: Doc Con for WSSB/OSD,
R. Shay

University of California
Lawrence Livermore Laboratory
P. O. Box 808
Livermore, CA 94550
Attn: Doc Con for:
L-156, R. Kalibjian
L-389, R. Ott
L-96, H. Kruger (Class L-94)
L-125, J. Keller
Technical Information Dept.

Office of Military Application
Department of Energy
Washington, DC 20545
Attn: Doc Con for Classified Library

Sandia Laboratories
P. O. Box 5800
Albuquerque, NM 87115
Attn: Doc Con for:
3141
J. Hood
F. Coppage
B. Gregory

Central Intelligence Agency
Washington, DC 20505
Attn: RD/SI, Rm 5G48, HQ Bldg.

Department of Transportation
Federal Aviation Administration
Headquarters Sec Div., ASE-300
800 Independence Ave., SW
Washington, DC 20591
Attn: ARD-350

Aerojet Electro-Systems Co.
Div. of Aerojet-General Corp.
P. O. Box 296
Azusa, CA 91702
Attn: SV/8711/70

Aerospace Corp.
P. O. Box 92957
Los Angeles, CA 90009
Attn: V. Josephson
I. Garfunkel
W. Willis
R. Crolius
J. Reinheimer

AVCO Research & Systems Group
201 Lowell Street
Wilmington, MA 01887
Attn: W. Broding

Battelle Memorial Institute
505 King Avenue
Columbus, OH 43201
Attn: R. Thatcher
R. Blazek
D. Hamman

BDM Corp.
P. O. Box 9274
Albuquerque International
Albuquerque, NM 87119
Attn: D. Alexander
Marketing

Bendix Corp.
Communication Division
East Joppa Road
Baltimore, MD 21204
Attn: Document Control

Bendix Corp.
Research Laboratories Division
Bendix Center
Southfield, MI 48075
Attn: M. Frank

Boeing Co.
P. O. Box 3707
Seattle, WA 98124
Attn: 8K-38
Aerospace Library
I. Arimura
R. Caldwell
C. Rosenberg

Booz-Allen and Hamilton, Inc.
776 Shrewsbury Avenue
Tinton Falls, NJ 07724
Attn: R. Chrisner

Brown Engineering Company, Inc.
Cummings Research Park
Huntsville, AL 35807
Attn: J. McSwain

California Institute of Technology
Jet Propulsion Lab
4800 Oak Grove Drive
Pasadena, CA 91103
Attn: J. Bryden
A. Stanley

Charles Stark Draper Lab., Inc.
555 Technology Square
Cambridge, MA 02139
Attn: K. Fertig
P. Kelly
R. Haltmaier
P. Greiff
H. Huemmler

Computer Sciences Corp.
1400 San Mateo Blvd., SE
Albuquerque, NM 87108
Attn: A. Schiff

Control Data Corp
P. O. Box O
Minneapolis, MN 55440
Attn: J. Meehan

Cutler-Hammer, Inc.
AIL Division
Comac Road
Deer Park, NY 11729
Attn: Cent Tech Files, A. Anthony

Dikewood Industries, Inc.
1009 Bradbury Drive, SE
Albuequerque, NM 87106
Attn: L. Davis

E-Systems, Inc.
ECI Division
P. O. Box 12248.
St. Petersburg, FL 33733
Attn: R. French

E-Systems, Inc.
Greenville Division
P. O. Box 1056
Greenville, TX 75401
Attn: Division Library

Effects Technology, Inc.
5383 Hollister Avenue
Santa Barbara, CA 93111
Attn: E. Steele

EX-Cal, Inc.
First National Bldg., E
Suite 1516
Albuquerque, NM 87108
Attn: R. Dickhaut

Fairchild Camera & Instrument Corp
464 Ellis Street
Mountain View, CA 94040
Attn: Sec Con for D. Myers

Fairchild Industries, Inc.
Sherman Fairchild Tech. Center
20301 Century Blvd.
Germantown, MD 20767
Attn: Mgr Config Data & Standards

University of Florida
Attn: Security Officer
P. O. Box 284
Gainesville, FL 32601
Attn: H. Sisler

Ford Aerospace & Communications
Ford & Jamboree Roads
Newport Beach, CA 92663
Attn: E. Poncelet, Jr.
K. Attinger
Tech Info Services

Ford Aerospace & Communications
3939 Fabian Way
Palo Alto, CA 94303
Attn: Technical Library
S. Crawford

General Electric Co.
Space Division
Valley Forge Space Center
P. O. Box 8555
Philadelphia, PA 19101
Attn: D. Tasca
D. Long
L. Jeffers
L. Chasen
J. Peden VFSC, Rm. 4230M
L. Sivo
J. Andrews

General Electric Co.
Re-Entry & Environmental Systems
P. O. Box 7722
Philadelphia, PA 19101
Attn: W. Patterson
J. Palchefsky, Jr.
Technical Library
R. Benedict

General Electric Co.
Ordnance Systems
100 Plastics Avenue
Pittsfield, MA 01201
Attn: J. Reidl

General Electric Co.
Aerospace Electronics Systems
French Road
Utica, NY 13503
Attn: C. Hewison

General Electric Co. - Tempo Cent.
for Advanced Studies
P. O. Drawer QQ
Santa Barbara, CA 93102
Attn: R. Rutherford
M. Espig
DASIAC

General Electric Co. - Tempo
Alexandria Office
Huntington Bldg., Suite 300
2560 Huntington Ave.
Alexandra, VA 22303
Attn: DASIAC

General Research Corp.
Santa Barbara Division
P. O. Box 6770
Santa Barbara, CA 93111
Attn: Tech Information Office

Georgia Institute of Technology
Georgia Tech Research Institute
Atlanta, GA 30332
Attn: R. Curry

Georgia Institute of Technology
Office of Contract Administration
Attn: Rsch Security Coordinator
Atlanta, GA 30332
Attn: Res & Sec Coord for H. Denny

Grumman Aerospace Corp.
S. Oyster Bay Road
Bethpage, NY 11714
Attn: J. Rogers

GTE Sylvania, Inc. - Electronics Sys.
Group - Eastern Division
77 A Street
Needham, MA 02194
Attn: L. Blaisdell
C. Thornhill, Librarian

GTE Sylvania, Inc.
189 B Street
Needham Heights, MA 02194
Attn: H&V Group
J. Waldron
P. Fredrickson

Harris Corp.
Electronics Systems Division
P. O. Box 37
Melbourne, FL 32901
Attn: C. Davis

Harris Corp.
Harris Semiconductor Division
P. O. Box 883
Melbourne, FL 32901
Attn: Mngr Linear Eng
T. Clark
Mngr Bipolar Digital Eng

Hazeltine Corp.
Pulaski Road
Greenlawn, NY 11740
Attn: Tech Info Ctr, M. Waite

Honeywell, Inc.
Avionics Division
2600 Ridgeway Parkway
Minneapolis, MN 55413
Attn: R. Johnson

Honeywell, Inc.
Avionics Division
13350 U.S. Highway 19, N.
St. Petersburg, FL 33733
Attn: MS 725-5

Honeywell, Inc.
Radiation Center
2 Forbes Road
Lexington, MA 02173
Attn: Technical Library

Hughes Aircraft Co.
Centinela and Teale
Culver City, CA 90230
Attn: K. Walker
CTDC, 6/E110
D. Binder

Hughes Aircraft Co.
El Segundo Site
P. O. Box 92919
Los Angeles, CA 90009
Attn: E. Smith, MS A620

IBM Corp.
Route 17C
Owego, NY 13827
Attn: Electromagnetic Compatability
Mono Memory Systems

Institute for Defense Analyses
400 Army-Navy Drive
Arlington, VA 22202
Attn: Tech Info Services

Ion Physics Corp.
S. Bedford Street
Burlington, MA 01803
Attn: R. Evans

IRT Corp.
P. O. Box 81087
San Diego, CA 92138
Attn: MDC
R. Mertz
Systems Effects Div.
Physics Div.

JAYCOR
205 S. Whiting Street, Suite 500
Alexandria, VA 22304
Attn: R. Sullivan
C. Turesko

Kaman Sciences Corp.
P. O. Box 7463
Colorado Springs, CO 80933
Attn: Dir Science & Tech Div
W. Rich
President
D. Bryce
W. Ware
J. Lubell

Litton Systems, Inc. - Guidance
and Control Systems Div.
5500 Canoga Avenue
Woodland Hills, CA 91364
Attn: W. Mras
J. Retzler

Lockheed Missiles & Space Co., Inc.
P. O. Box 504
Sunnyvale, CA 94086
Attn: E. Smith
B. Kimura
L. Rossi
S. Taimuty
D. Wolfhard

Lockheed Missiles & Space Co., Inc.
3251 Hanover Street
Palo Alto, CA 94304
Attn: Tech Info Ctr, D/Coll
Reports Library

M.I.T. Lincoln Lab
P. O. Box 73
Lexington, MA 02173
Attn: L. Loughlin
Library, A-082

Martin Marietta Corp.
Orlando Division
P. O. Box 5837
Orlando, FL 32805
Attn: TIC/MP-30

Martin Marietta Corp.
Denver Division
P. O. Box 179
Denver, CO 80201
Attn: P. Kase
Goodwin
Research Library

McDonnell Douglas Corp.
P. O. Box 516
St. Louis, MO 63166
Attn: Library
T. Ender

McDonnell Douglas Corp.
5301 Bolsa Avenue
Huntington Beach, CA 92647
Attn: P. Albrecht

Mission Research Corp.
P. O. Drawer 719
Santa Barbara, CA 93102
Attn: M. Van Blaricum

Mission Research Corp.
EM System Applications Div.
1400 San Mateo Blvd. SE, Suite A
Albuquerque, NM 87108
Attn: David E. Merewether

Mission Research Corp. - San Diego
P. O. Box 1209
La Jolla, CA 92038
Attn: J. Raymond
V. A. J. Van Lint

National Academy of Sciences
Committee on Atmospheric Sciences
2101 Constitution Avenue, NW
Washington, DC 20418
Attn: R.Shane

University of New Mexico
Electrical Eng & Computer Science
Department
Albuquerque, NM 87131
Attn: Harold Southward

Northrop Corporation
Northrop Research & Tech Center
One Research Park
Palos Verdes Peninsula, CA 90274
Attn: J. R. Srour
S. Othmer
Library

Palisades Inst for Rsch Services, Inc.
201 Varick Street
New York, NY 10014
Attn: Secretary

Physics International Co.
2700 Merced Street
San Leandro, CA 94577
Attn: J. Shea

Power Conversion Technology, Inc.
11588 Sorrento Valley Road
San Diego, CA 92121
Attn: V. Fargo

R & D Associates
P. O. Box 9695
Marina del Rey, CA 90291
Attn: W. Karzas
C. MacDonald

R & D Associates
1401 Wilson Blvd., Suite 500
Arlington, VA 22209
Attn: J. Bombardi

Raytheon Co.
Hartwell Road
Bedford, MA 01730
Attn: G. Joshi

Raytheon Co.
528 Boston Post Road
Sudbury, MA 01776
Attn: H. Flescher

RCA Corp. - Government Systems
Division - Astro Electronics
P. O. Box 800, Locust Corner
East Windsor Township
Princeton, NJ 08540
Attn: G. Brucker

RCA Corp.
David Sarnoff Research Center
P. O. Box 432
Princeton, NJ 08540
Attn: D. O'Connor
G. Hughes

Rensselaer Polytechnic Institute
P. O. Box 965
Troy, NY 12181
Attn: R. Ryan
R. Gutmann

Research Triangle Institute
Attn: Security Officer
P. O. Box 12194
Research Triangle Park, NC 27709
Attn: Eng Div, Mayrant Simons, Jr.

Rockwell International Corp.
P. O. Box 3105
Anaheim, CA 92803
Attn: James E. Bell, MS HA10
K. Hull
N. Rudie

Rockwell International Corp.
Space Division
12214 S. Lakewood Blvd.
Downey, CA 90241
Attn: TIC D/41-092 AJ01
D. Stevens

Rockwell International Corp.
815 Lapham Street
El Segundo, CA 90245
Attn: TIC BA08

Sanders Associates, Inc.
95 Canal Street
Nashua, NH 03060
Attn: M. Aitel
L. Brodeur

Science Applications, Inc.
P. O. Box 2351
La Jolla, CA 92038
Attn: L. Scott
J. Beyster

Science Applications, Inc.
Huntsville Division
2109 W. Clinton Avenue, Suite 700
Huntsville, AL 35805
Attn: N. Byrn

Singer Co. - Data Systems
150 Totowa Road
Wayne, NJ 07470
Attn: Tech Info Center

Sperry Rand Corp.
Sperry Division
Marcus Avenue
Great Neck, NY 11020
Attn: C. Craig
P. Maraffino
R. Viola

Sperry Rand Corp.
Sperry Flight Systems
P. O. Box 21111
Phoeniz, AZ 85036
Attn: D. Andrew Schow

Spire Corp.
P. O. Box D
Bedford, MA 01730
Attn: Roger G. Little

SRI International
333 Ravenswood Avenue
Menlo Park, CA 94025
Attn: P. Dolan

Tetra Tech, Inc.
1911 Fort Myer Drive
Arlington, VA 22209
Attn: T. Simpson

Texas Instruments, Inc.
P. O. Box 6015
Dallas, TX 75265
Attn: D. Manus

TRW Defense & Space Sys. Group
One Space Park
Redondo Beach, CA 90278
Attn: O. Adams (2)
H. Holloway
R. Plebuch
A. Narevsky
Technical Info Center
Vulnerability & Hardness Lab
R. Webb

TRW Defense & Space Sys. Group
San Bernardino Operations
P. O. Box 1310
San Bernardino, CA 92402
Attn: F. Fay
R. Kitter

Vought Corp.
P.O. Box 225907
Dallas, TX 75265
Attn: Technical Data Center
Library
R. Tomme

Westinghouse Electric Corp.
Defense & Electronic Systems Ctr.
P. O. Box 1693
Baltimore-Washington Intl Airport
Baltimore, MD 21203
Attn: MS 3330